Nanoscale

PAPER

Check for updates

Tailoring the structural and electro-optical properties of avisible-light emitting BaZrO₃ photocatalyst: integrating DFT and comprehensive experimental analysis†

Shubha Dubey, ID *[a] Vipin Kumar, ID *[b,c] Kumud Dubey,[a] Chinmay Sahu,[a] Anchit Modi,[d] U. K. Gautam,[e] R. K. Sharma,[e] Fozia Z. Haque, ID [f] Gitanjali Pagare[g] and N. K. Gaur[a]

In the present work, the synthesis of BaZrO₃ nano-ceramics is explored through flash combustion utilizing glycine as a fuel. The resulting nanoparticles exhibit a cubic *Pm3̄m* space group and a spherical morphology with an average size of 45.31 nm. XRD and EDAX verify the integrity of the phase. FTIR and Raman spectroscopy is used to analyze the molecular bonds and their vibrations, while XPS reveals surface compositions and oxidation states. The electro-optical properties of BaZrO₃ are explored through UV-Vis spectroscopy and electronic band structure analysis. The Tauc plot displays a pair of band gaps, with values of 3.08 eV and 3.84 eV, corresponding to indirect and direct characteristics. BaZrO₃ demonstrates photocatalytic potential with a degradation efficiency of approximately 36.41% for rhodamine B under visible light. Electronic band structure analysis reveals an indirect band gap of 3.05 eV in BaZrO₃. The Bader analysis emphasizes the pronounced covalent characteristics present in the Zr−O bond. Photoluminescence spectra exhibit electronic transitions with a peak observed at 420.57 nm (~2.94 eV), suggesting activity within the violet light spectrum. The CIE chromaticity coordinates imply prospective uses in the manufacture of violet-blue LEDs. These findings underscore the tailored properties of BaZrO₃ nano-ceramics, showcasing their versatility for various applications, notably in advanced optoelectronic devices.

[a]*Department of Physics, Barkatullah University, Bhopal, 462 026, India. E-mail: shubha.dubey4@gmail.com*
[b]*Department of Physical Electronics, School of Electrical Engineering, Tel Aviv University, Tel Aviv 699 780, Israel. E-mail: vipinkumar@mail.tau.ac.il, vipinkumar0247@gmail.com*
[c]*The Sackler Center for Computational Molecular and Materials Science, Tel Aviv University, Tel Aviv 699 780, Israel*
[d]*Department of Basic Sciences, IITM, IES University, Bhopal, 462 044, India*
[e]*Technical Physics Division, Bhabha Atomic Research Centre, Mumbai, 400 085, India*
[f]*Department of Physics, Maulana Azad National Institute of Technology, Bhopal, 462 003, India*
[g]*Department of Physics, Sarojini Naidu Govt. Girls PG Autonomous College, Bhopal, 462016, India*
†Electronic supplementary information (ESI) available. See DOI: https://doi.org/10.1039/d4nr00517a VK Current Address- Surface Science Laboratory, Department of Materials and Earth Sciences, Technical University of Darmstadt, Otto-Berndt-Straße 3, 64287 Darmstadt, Germany. E-mail: vkumar@surface.tu-darmstadt.de

1. Introduction

The modification of source materials across atomic and molecular levels has enabled the development of a wide range of nanoscale materials, allowing for the synthesis of metal–oxide nanoparticles with improved characteristics.[1] The unique properties and potential applications of metal–oxide nanoparticles have sparked curiosity, leading to increased interest in various fields such as health, electronics, and energy.[2] Moreover, the multifaceted applications and distinct characteristics exhibited by transition metal semiconductors in the realms of optoelectronics and energy sectors have garnered considerable interest across a spectrum of fields. Within this category of nanoparticles, transition metal semiconductors stand out prominently, fulfilling pivotal functions in magnetic storage media, catalytic processes, and gas detection systems. Additionally, metal–oxide nanoparticles hold promise for applications in electronic devices, solid oxide fuel cells, and optical materials. Research into metal oxide nanoparticles is ongoing, driven by their unique material properties and their potential utility in various domains.[3] Metal oxides with the structure of a perovskite are frequently used in chemical sensors, solid oxide fuel cells, thermoelectric devices, and oxygen-permeable membranes, among other applications.[4,5] Perovskites indicated by the chemical formula XYO₃ (where X denotes alkaline earth and Y signifies 3d transition metals)

demonstrate outstanding properties as both structural and electronic ceramics.[6] When appropriately modified with dopants, these substances demonstrate conductivity in either ionic or electronic forms. Typically, in XYO_3 compounds, the valence band (VB) near the Fermi energy level (E_f) is typically formed by the 2p orbitals of oxygen atoms. At the same time, the formation of the conduction band involves the contribution of d orbitals from the Y atom. The level of interaction between Y and O is contingent upon the electronegativity of the Y atom. As a result, the characteristics of the Y-site component have a significant impact on the photocatalytic capabilities of perovskite materials.

Among the several perovskite nanoparticle varieties, attention has shifted to $BaZrO_3$ nanoparticles due to their ability to emit visible light, making them useful in optical displays and devices.[7] $BaZrO_3$ nanoparticles have particular appeal in the realm of optoelectronics owing to their robust efficiency and stability across diverse operational conditions. Furthermore, nanomaterials such as $BaZrO_3$ have unique properties that surpass many standard bulk materials in terms of efficiency and resilience.[8,9] Additionally, studies suggest that the $BaZrO_3$ nanoparticles can be used in catalysis, since they have catalytic properties across a wide range of chemical reactions. These nanoparticles not only possess optical prowess but also remarkable traits, such as a simple cubic perovskite structure, demonstrating high chemical stability, exceptional mechanical strength, and resilience to extreme temperatures. These features broaden their utility in fabricating heat-resistant composites. Recent research has unveiled the potential of $BaZrO_3$ nanoparticles as proton conductors.[10,11] Zhu and fellow researchers conducted a study aimed at accelerating proton conduction in yttrium (Y)-doped barium zirconate ($BaZrO_3$) through the manipulation of oxygen vacancies. This approach involves engineering these vacancies, primarily achieved by introducing calcium (Ca) doping, with the goal of enhancing proton diffusion within the material.[12] The functionality of semiconductor devices, encompassing photon absorption or emission, solid-state lighting, photovoltaic cells, detectors, displays, sensors, lasers, and photocatalysts, is substantially impacted by the bandgap.[13] The $BaZrO_3$ perovskite stands as a promising material across diverse applications, ranging from fuel cells to solar photovoltaics, owing to its notable oxide-ion conductivity.[14]

The bandgap, a fundamental property of semiconductor materials, profoundly influences the functionality of semiconductor devices by imparting unique electrical characteristics essential for modern electronics. It defines the energy distinction between the valence band, where electrons are bound to specific atoms, and the conduction band, housing free electrons capable of mobility within the material, consequently dictating the material's electrical conductivity and optical properties and requiring precise control and modification. Nevertheless, $BaZrO_3$'s broad bandgap limits its photoactivity and ability to absorb photons in the visible light spectrum.[15] Consequently, modifying $BaZrO_3$'s bandgap has become a key area of research to enhance its effectiveness in

photovoltaic and related applications. For example, Patra et al. achieved significant improvements in photocatalytic performance by modifying $BaZrO_3$ with carbon dots, demonstrating superior efficiency with an optimal CD loading.[6] Various methods have been employed to synthesize $BaZrO_3$ in different sizes and shapes, such as polyhedra, nanocubes, nanowires, decaoctahedra, and monodispersed particles.[16,17] These efforts have enhanced its optical, ferroelectric, and electronic properties. Common synthesis techniques include the solid-state reaction (SSR), one-step auto-combustion, sol–gel, precipitation, hydrothermal, and green synthesis techniques, which are widely used to produce $BaZrO_3$ nanoparticles.[7,9] Modifying the bandgap of $BaZrO_3$ often involves doping and alloying with specific elements, introducing impurity energy levels into its band structure. This precise synthesis not only affects the size, shape, and composition but also unlocks potential applications in catalysis and microwave technology.[18,19] Efforts to enhance visible light absorption in these wide bandgap materials include adjusting their band positions with alternative elements or modifying anions to create oxygen-related vacancies in the lattice structure. Ullah et al. used DFT calculations to analyze the properties of pristine and Cd-substituted $BaZrO_3$, finding that Cd-substitution significantly enhanced optical performance, making it more efficient for optoelectronic devices. Both pure and Cd-substituted $BaZrO_3$ showed potential for efficient overall water splitting, indicating their suitability for green energy applications and solar cells.[20] Kayathiri et al.'s green synthesis narrowed $BaZrO_3$'s bandgap to 4.01 eV through plant chemical substitution, improving its properties. They reported an 84.1% maximum degradation efficiency of CR dye after 90 minutes of light irradiation.[9]

However, diverging from traditional doping approaches, an alternative method has been employed in this case, involving modified synthesis techniques, optimized sintering temperatures, and the creation of oxygen vacancies within the lattice.[21] High-temperature synthesis techniques offer a means to fine-tune semiconductor bandgaps by tailoring interfacial energetics, adjusting valence and conduction band edges, and inducing surface oxygen vacancies. Surface oxygen voids function as traps for optically generated charge carriers, lessening the likelihood of electron–hole recombination, while bulk oxygen vacancies serve as centers for the recombination of photogenerated charges, significantly impacting photocatalysis.[22] In addition, the material experiences the development of mid-gap energy levels as a consequence of these trap states, enabling precise adjustments to the electronic structure. The bandgap values achieved through various synthesis techniques are summarized in Table 1 for a comprehensive comparison.

Our study introduces a novel approach to synthesizing and characterizing $BaZrO_3$ that significantly advances the current understanding and potential applications of this material. We have developed an innovative synthesis method that allows for precise control over both particle size and morphology, addressing scalability and uniformity challenges prevalent in conventional techniques. Moreover, our thorough investigation into

Table 1 Comparison of bandgap values achieved through various synthesis techniques for $BaZrO_3$

S. No.	Composition	Synthesis technique	Sintering temperature	Band gap (eV)	Particle size (nm)	Morphology	Ref.
1	$BaZr_{1-x}Ce_xO_3$ ($x = 0.00$–0.04)	Modified hydrothermal method	100 °C	2.37–2.14	~150–200	Hollow spheres	6
2	$BaZrO_3$	CHM approach	50 °C	—	50–240	Nano cubes	23
3	$BaZrO_3$	Co precipitation method	110 °C	4.87	200	Spheres	24
4	$BaZrO_3$	Chemically synthesized	400 °C	4.28	16	Non-uniform nanoparticles	9
5	$BaZrO_3$	Green synthesized	400 °C	5.3	11	Non-uniform nanoparticles	9
6	$BaZrO_3$	Pechini-type process	1100 °C	4.8	—	—	25

impurity phases, employing advanced techniques such as Raman spectroscopy and XPS, provides a deeper understanding of the synthesis process and its implications for materials properties, a level of analysis rarely explored in the existing literature. Crucially, we have demonstrated the capability to finely tune the bandgap of $BaZrO_3$ through careful adjustment of synthesis parameters, essential for optimizing performance in optoelectronic devices. Departing from traditional doping strategies, our approach involves modified synthesis techniques and optimized sintering temperatures to deliberately introduce oxygen vacancies within the lattice, thereby enhancing semiconductor properties. This comprehensive synthesis and characterization approach not only advances fundamental knowledge but also positions $BaZrO_3$ for innovative applications in fields ranging from electronics to catalysis.

Presently, the aim is to tailor the band gap of barium zirconate using suitable synthesis techniques to explore its potential as a photocatalyst for degrading rhodamine B dye and perform a detailed structural, electronic and optical analysis by means of different spectroscopic techniques. Density functional theory calculations, utilizing the projector augmented wave (PAW) method, are employed to confirm the origin of the optical band gap. Bader charge analysis is also performed in order to achieve a quantitative assessment of the bonding characteristics in the $BaZrO_3$ ceramic.

2. Experimental and computational details

2.1 Synthesis

High-purity barium nitrate $[Ba(NO_3)_2]$ and zirconium dioxide $[ZrO_2]$ nanoparticles were used as an oxidizer, while glycine $[C_2H_5NO_2]$ was used as a fuel in a proportion of $0.1 : 0.1 : 0.22$ for a one-step facile flash combustion synthesis. The proportional quantities of these materials were determined based on the following chemical equation:

$$9Ba(NO_3)_2 + 9ZrO_2 + 10C_2H_5NO_2 \rightarrow 9BaZrO_3 + 20CO_2 \uparrow + 25H_2O + 14N_2 \uparrow \tag{1}$$
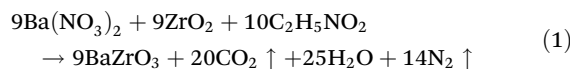
The main steps for the one-step facile flash combustion synthesis are schematically illustrated in Fig. 1. The appropriate amount of oxidizers and fuel was taken in a 100 ml beaker and mixed together to form a homogeneous mixture. A sufficient amount of glycine solution was added to ensure that the total number of reducing and oxidizing valences was equal, resulting in an equivalence ratio (oxidizing valences/reducing valences) of one. This served to maximize the release of heat due to the exothermic reaction.

The obtained homogeneous mixture was then aged overnight at room temperature to form a xerogel. Subsequently, the xerogel was placed on a hotplate and maintained at a temperature of around 200 °C. During this stage, the xerogel underwent dehydration and self-propagating combustion within a few seconds, accompanied by a flash of light. This combustion reaction released CO_2 and N_2 gases and formed a porous foamy-fluffy powder due to the exothermic reaction between the oxidizer and fuel. The resulting porous foamy-fluffy powder of $BaZrO_3$ was reheated at 250 °C for 4 hours. Afterward, the fluffy powder was ground for 2 hours and calcined at 1200 °C in air for 12 hours using a tubular furnace. Finally, the $BaZrO_3$ powder was reground and sintered at 1200 °C under the same conditions and for the same duration to enhance its crystallinity.

2.2 Characterization

The determination of the phase composition and crystal structure of the prepared $BaZrO_3$ nanoparticle is accomplished using powder X-ray diffraction (PXRD) with CuKα radiation ($\lambda = 1.54056$ Å) on the Bruker D8 Advance instrument. FullProf software was used for diffractogram analysis, utilizing the pseudo-Voigt function to refine peak profiles. Characterization of the sample size, surface morphology, and elemental composition was carried out using a "Carl Zeiss Supra 55" FESEM, combined with energy X-ray dispersive spectroscopy (EDS). The standard KBr pellet technique was used to record the Fourier transform infrared (FT-IR) absorption spectrum, using a PerkinElmer FT-IR spectrometer (Spectrum 1000, Japan). For Raman spectra, the LaBRAM HR Raman spectrometer from Horiba (France SAS), utilizing a 633 nm He–Ne laser source with 100% power, was employed. X-ray photoelectron spectroscopy (XPS) was performed at the Indus-2 synchrotron facility RRCAT Indore, operating in the hard X-ray region and utilizing a Photoemission Electron Spectrometer (PES), BL-14, powered by a 1.5 T bending magnet source. This synchrotron source is equipped with a double-crystal monochromator [Si (111)] featuring an excitation energy of 4.065 keV. The system is further enhanced with a hemispherical analyzer and detector system (Phoibos 225, Specs make). Throughout the experi-
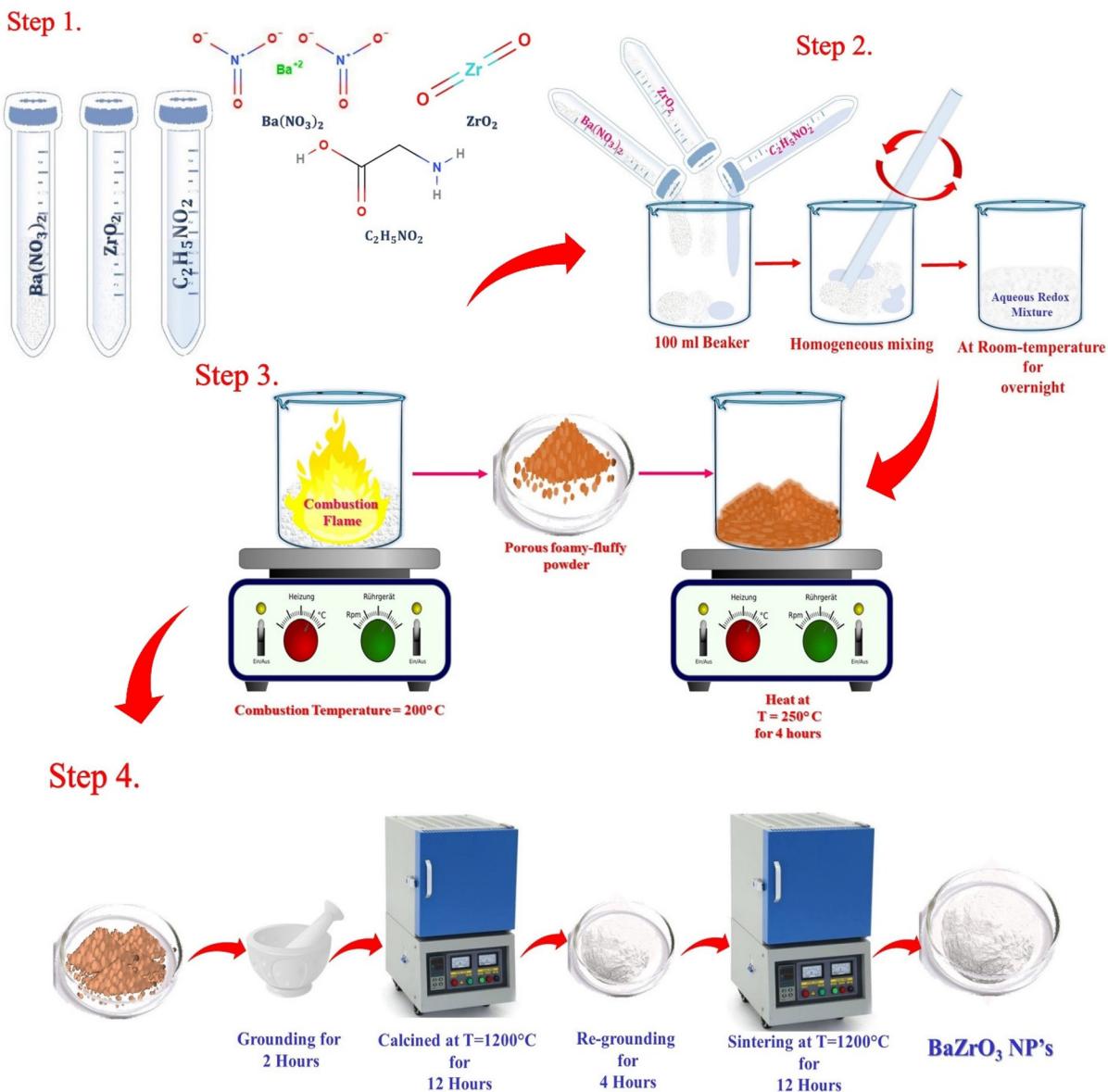
Fig. 1 Schematic diagram of the synthesis of BaZrO₃ nanoparticles *via* glycine-assisted combustion techniques.

ments, the pressure in the experimental station was maintained at 5×10^{-9} mbar.

To address surface charging effects, all peaks were referenced to the C 1s spectrum (284.77 eV) in the analysis. The XPS core level spectral data underwent analysis and quantification using XPSPEAK 4.1 software, and the Shirley background method was applied to subtract the background from all XPS spectra. All measurements were conducted at room temperature.

Polarization measurements were performed using ferroelectric hysteresis loops (M/s Radiant Technology, USA) at 20 kHz. The optical band study of synthesized BaZrO₃ nanoparticles was carried out using a PerkinElmer Lambda 950 UV-visible spectrophotometer across a wavelength range of 200 to 800 nm. Photocatalytic activity testing of the BaZrO₃ catalyst

for RhB (10 mg L⁻¹) degradation was conducted under UV light using a 150 W Xenon lamp housed within a column-shaped stainless-steel cabinet (λ_{max} ~400 nm). Room temperature photoluminescence excitation spectra were acquired using an F-7000 Hitachi fluorescence spectrophotometer, utilizing a Xenon lamp employed as the excitation source for emission.

2.3 Computational details

In this study, electronic and geometrical calculations based on density-functional theory (DFT) were conducted using the Vienna *ab initio* simulation package (VASP).[26] The projector-augmented wave (PAW) method was employed to consider both ionic core effects and electron–electron interactions.[27] The Perdew–Burke–Ernzerhof (PBE) functional within the generalized gradient approximation (GGA) handled the exchange–

correlation potential.[28] To ensure precision in both geometrical and electronic properties, a kinetic cut-off energy of 550 eV was specified. Optimization and partial density of states analysis utilized a 15 × 15 × 15 dense k-point mesh employing the Monkhorst–Pack (MP) system.

3. Results and discussion

3.1 Crystal structure and phase composition analysis

3.1.1 X-Ray diffraction pattern.
For an initial assessment of the crystallographic structure, its lattice parameters, and size of the BaZrO$_3$ nanoparticles that were prepared, we utilized the X-ray diffraction technique. The analysis was conducted at room temperature, employing a wide range of Bragg's angles (2θ) spanning from 20° to 90°. The first peak at 2θ of 21.18°

Fig. 2 XRD patterns of the as-synthesized BaZrO$_3$ nanoparticles.

was indexed with the (100) planes, confirming a cubic cell structure for BaZrO$_3$. The complete hkl assignment, detailed in Fig. 2, aligns with JCPDS card number 00-001-0890.[29,30] However, one peak around 23.96 degrees suggests the presence of BaCO$_3$ as an impurity.[29] The emergence of the BaCO$_3$ phase is likely attributed to the reaction between BaO and CO$_2$. It is plausible that BaCO$_3$ is formed during the breakdown of the intermediate –(COO)$_2$Ba functional groups. Clearly, the crystallinity shows a noticeable enhancement following the heating of the porous foamy-fluffy powder of BaZrO$_3$. In Fig. 3(a), the fitting process of the XRD pattern of the BaZrO$_3$ nanoparticles using the Rietveld method within a perovskite framework characterized by a cubic configuration in the $Pm\bar{3}m$ (no. 221) space group is presented. The fitting resulted in a final difference and a profile fit. The XRD profile reveals three prominent peaks at 30°, 43°, and 53° with Miller indices (1 1 0), (2 0 0), and (2 1 1), respectively. These observations suggest that the crystal structure is predominantly oriented in the (1 1 0), (2 0 0), and (2 1 1) directions. The calculated pattern and the observed one exhibit a strong correspondence with characteristics atomic parameters after Rietveld refinement are presented in Table 2. The low values of various R-factors such as R_{exp}, R_{bragg}, R_p, R_F, R_{wp}, and χ^2, along with GOF, support the justification for the refined model, indicating a well-aligned agreement between the experimental data and the refined model.

The Williamson–Hall plot method[31] was employed to determine the crystallite sizes of the synthesized samples through the following relationship:

$$\beta \cos \theta = 4\varepsilon \sin \theta + k\lambda/D \qquad (2)$$

where K is the Scherrer constant, often taken as 0.9, D stands for the crystallite size, λ represents the X-ray radiation wave-
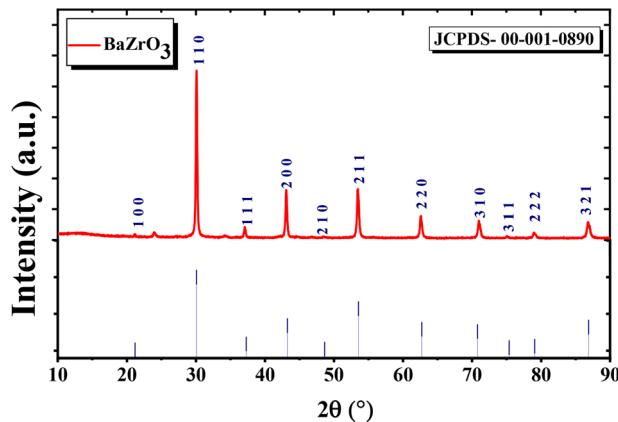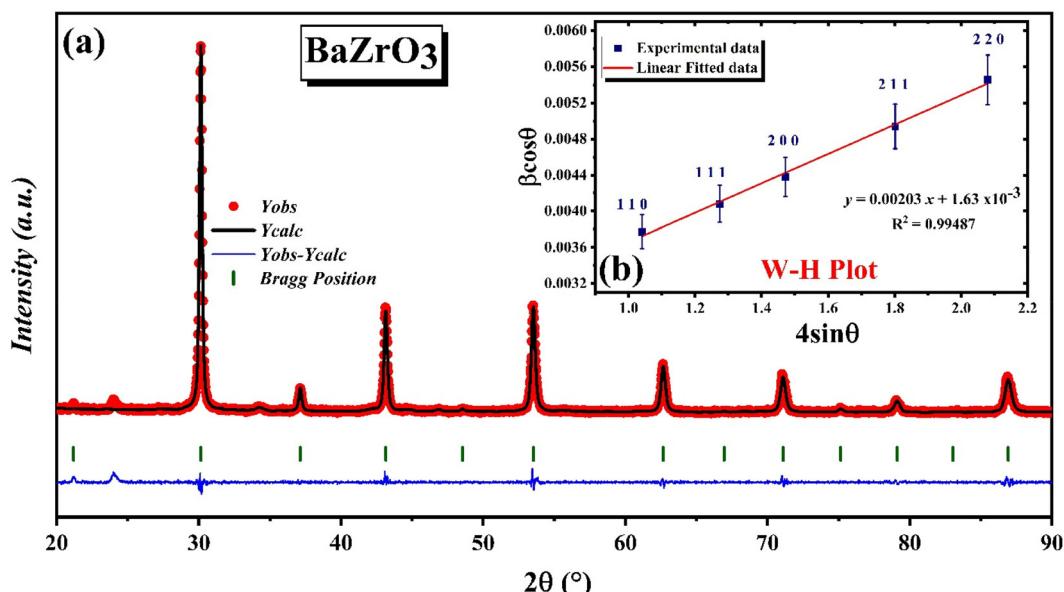

Fig. 3 (a) Rietveld refined X-ray diffraction pattern of BaZrO$_3$ nanoparticle and (b) W–H plot.

Table 2 Structural and lattice parameters, elemental composition, and effective Bader charges of Ba, Zr and O atoms in the pristine $BaZrO_3$ ceramic

Phase	$BaZrO_3$				
Structural & lattice parameters					
Space group	$Pm3m$ (221)				
a (Å)	4.18990				
Atoms	Atom	Site/Sym.	x	y	z
	Ba	$1b/m\bar{3}m$	0.5	0.5	0.5
	Zr	$1a/m\bar{3}m$	0.0	0.0	0.0
	O	$3d/4/$ $mm \cdot m$	0.5	0.0	0.0
V (Å³)	73.5500				
D (nm)	70.2900				
ε (×10⁻³)	1.6200				
$\langle d_{Ba-O}\rangle$ (Å)	2.96270				
$\langle d_{Zr-O}\rangle$ (Å)	2.09494				
Reliability	R_p	14.70			
factors	R_{wp}	14.70			
	R_{exp}	13.94			
	R_{Bragg}	1.805			
	R_f	1.930			
	χ^2	1.120			
	GOF	1.054			
Elemental composition for $BaZrO_3$					
Element		Weight %	Atomic %	Error %	
C K		17.1	45.3	11.4	
O K		18.7	37.2	9.6	
Zr L		22.2	7.8	5.5	
Ba L		42.0	9.7	7.8	
Total		100.00	100.00	34.3	
Effective Bader charges					
Atom		Effective Bader charge (e)			
Ba^{2+}		1.5229			
Zr^{4+}		2.4952			
O^{2-}		−1.3394			

length (λ = 1.5406 Å), θ corresponds to Bragg's angle, β signifies the full width at half-maximum (FWHM) of the Bragg's peak, and ε denotes the internal strain. The calculation of crystallite size (D) involves determining the Y-intercept of the linear fit, while the lattice strain can be represented by the slope of the linear line. Fig. 3(b) presents an illustrative Williamson–Hall plot for the $BaZrO_3$ sample. According to the Hall–Williamson method, the calculated crystallite size for the predominant ($h\;k\;l$) Bragg reflection depicted in Fig. 3(b) is 70.29 nanometers. The value of internal strain is tabulated in Table 1.

In Fig. S1(a),† we depict the crystallographic representation of $BaZrO_3$ nanoparticles, emphasizing their perovskite nature characterized by a robust cubic symmetry. In this crystalline arrangement, the central positions are occupied by Ba atoms, with Zr atoms positioned at the unit cell's vertices. Furthermore, oxygen atoms are situated at the midpoint of the edges. Notably, the Ba cations exhibit a 12-fold octahedral coordination, while the Zr cations display a 6-fold octahedral coordination, as illustrated in Fig. S1(b) and S1(c),† respectively, (ESI†).

The analysis of $BaZrO_3$ charge density plots offers crucial insights into its electronic structure and bonding traits. An in-depth examination of the electron density distribution within

the unit cell involved conducting a detailed study that mapped electron density in the 110 plane using the GFourier program,[32] which is a component of the FullProf package. This method generated two-dimensional Fourier maps, effectively illustrating how electron density envelops each atom in the compound's elements.

Typically depicted with contour lines, these maps offer a clear and intuitive view of electron density distribution. Shown in Fig. S1(d and e),† the color scale in these maps illustrates varying electron density levels. Areas of higher electron density appear in shades of red, while lower density regions are depicted in violet. Significantly, there is a notable elevation in electron density for all atoms except oxygen and the interstitial region. This visual representation effectively illustrates unique electron density patterns for various atoms in the compound, unveiling localized electron distribution and highlighting significant density regions within the crystal structure. From the Pauling electronegativity scale,[33] the Ba–O and Zr–O bonds exhibit a more ionic character. Moreover, predominant charge transfer occurs from other atomic species towards the oxygen atoms. Additionally, the Ba–O bond appears more ionic compared to the Zr–O bond.

3.1.2 Structural morphology and chemical composition analysis. A microscopic investigation employing Field Emission Scanning Electron Microscopy (FESEM) and Energy Dispersive X-ray Analysis (EDAX) was conducted to validate the microstructural features and dimensions of the $BaZrO_3$ nanoparticles. In Fig. 4(a and b), the FESEM micrographs at 100 nm for the $BaZrO_3$ nanoparticles are displayed. The sample showcases a homogeneous dispersion of particles characterized primarily by agglomerates of nanocrystals, assuming a spherical morphology. This distinct morphology, attributed to the utilization of the wet-chemical technique,[34] serves as an indicator of a densely packed particle arrangement. This agglomeration phenomenon is frequently encountered, particularly when synthesis is conducted at elevated temperatures.[35]

Fig. 4(c) presents the distribution of average particle sizes, with a frequency plot illustrating the size distribution derived from measurements of a substantial quantity of $BaZrO_3$ particles. The particle size distribution conforms to the characteristics of a normal distribution function. Notably, the calculated average particle size of $BaZrO_3$ stands at approximately 45.31 nm. Previously, $BaZrO_3$ powder was synthesized using sol–gel auto-combustion in a pre-heated furnace, exploring the influence of pH variation on citrate nitrate sol-gels and resulting in nanoparticles averaging 33.3 nm in size.[36] In order to establish the elemental composition of $BaZrO_3$, Energy Dispersive X-ray Analysis (EDAX) was performed under precisely controlled temperature conditions. The EDAX spectrum depicted in Fig. 4(d) distinctly exhibits the detection of Ba, Zr, and O elements, thus confirming the absence of any significant loss of essential elements during the sintering process, accounting for experimental uncertainties. The elemental composition typical of $BaZrO_3$, involving atomic percentage, is presented in Table 2. This meticulous analytical evaluation
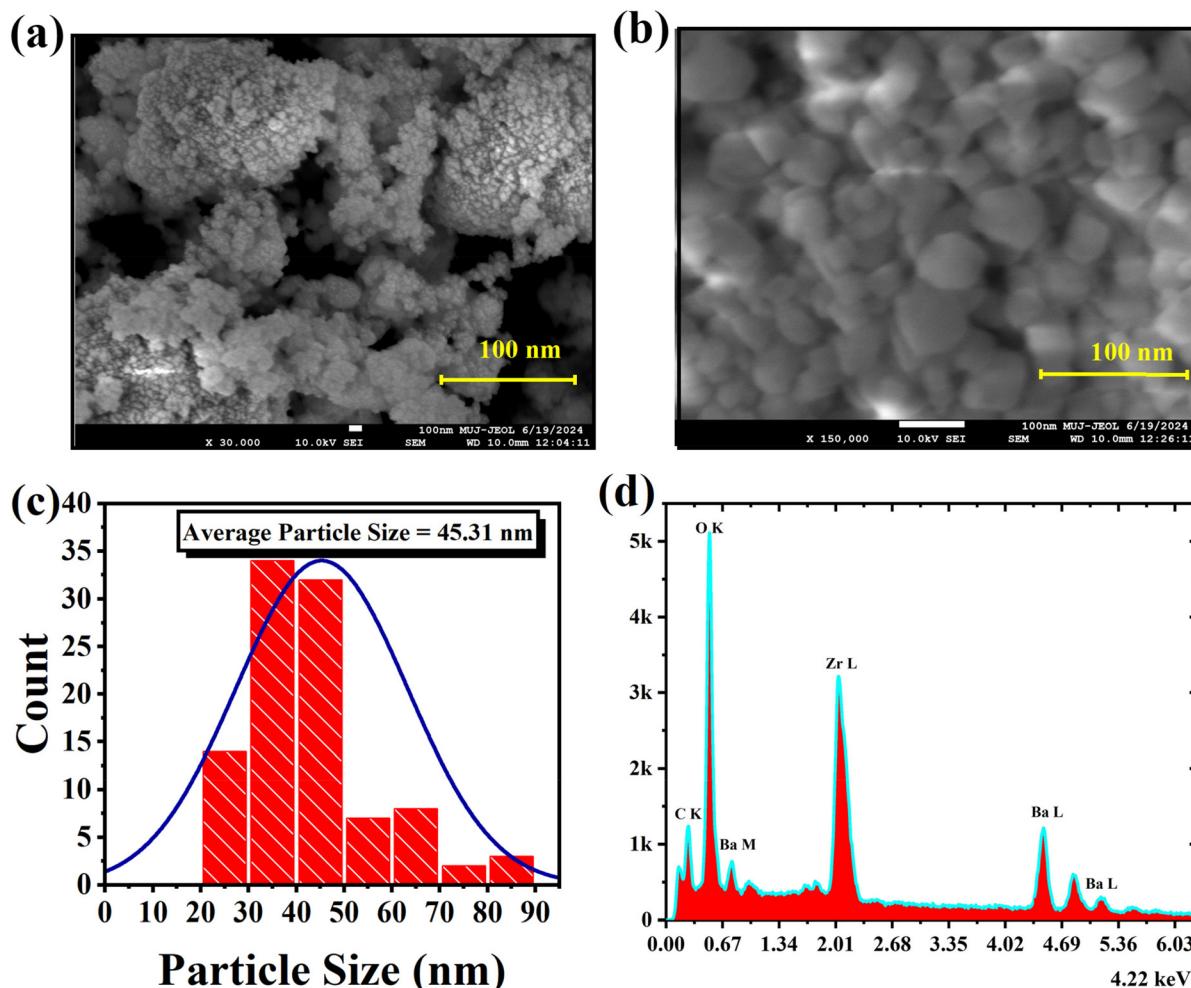
Fig. 4   (a and b) Surface morphology micrographs, (c) average particle size distribution of BaZrO₃, and (d) EDAX spectra.

reinforces both the consistency in cationic composition within BaZrO₃ and the non-existence of secondary phases within the structure of BaZrO₃. The observation reveals a Ba/Zr ratio of 1.24, nearly approaching unity, signifying the integration of these elements into the structure and providing confirmation of the absence of any remaining oxides.[37]

Furthermore, for a thorough comprehension of the elemental composition and distribution within the synthesized nanoparticles, we have incorporated the elemental distribution graphs derived from EDS analysis as depicted in Fig. S2.† The EDS mapping data, shown in Fig. 5(a–d), highlights the following: Fig. 5(a) identifies the region where the EDS mapping was conducted, while Fig. 5(b–d) respectively displays the presence of Ba, Zr, and O in the synthesized sample. Importantly, no other detectable impurities were found within the resolution limit of the EDS measurement.

3.1.3   Phonon dispersion curve. Examining thermodynamic stability involved calculating phonon dynamics while assuming the cubic $Pm\bar{3}m$ phase. Fig. S3† illustrates phonon dispersion relations along the principal symmetry directions of the Brillouin zone. A noteworthy aspect of the phonon spectra

is the lowest-frequency phonon branch, which demonstrates negative phonon frequencies at the M-points within the Brillouin zone. The unstable phonon mode at the M-point, which was not observed by Perrichon and coworkers[38] or Bilic *et al.*,[39] was detected in other calculations reported by Helal *et al.*[40] and Akbarzadeh,[41] which also employed the DFT method. The occurrence of phonon instability at the M-point is contingent upon the selection of the exchange–correlation potential and pseudopotential quality used to depict the interaction between the core and the valence electrons.[42]

Imaginary frequencies, denoted by negative phonon frequencies, signify a breakdown in crystal symmetry. Anharmonic phonon interactions can also contribute to these negative frequencies, potentially triggering a structural phase transition in BaZrO₃ under specific conditions. It is crucial to emphasize that the computed phonon dispersion spectra correspond to conditions of absolute zero temperature and zero pressure. Variations in temperature or pressure can significantly alter the situation. Thus, it can be inferred that BaZrO₃ displays dynamic instability at low temperatures and zero pressure. However, this scenario may change under
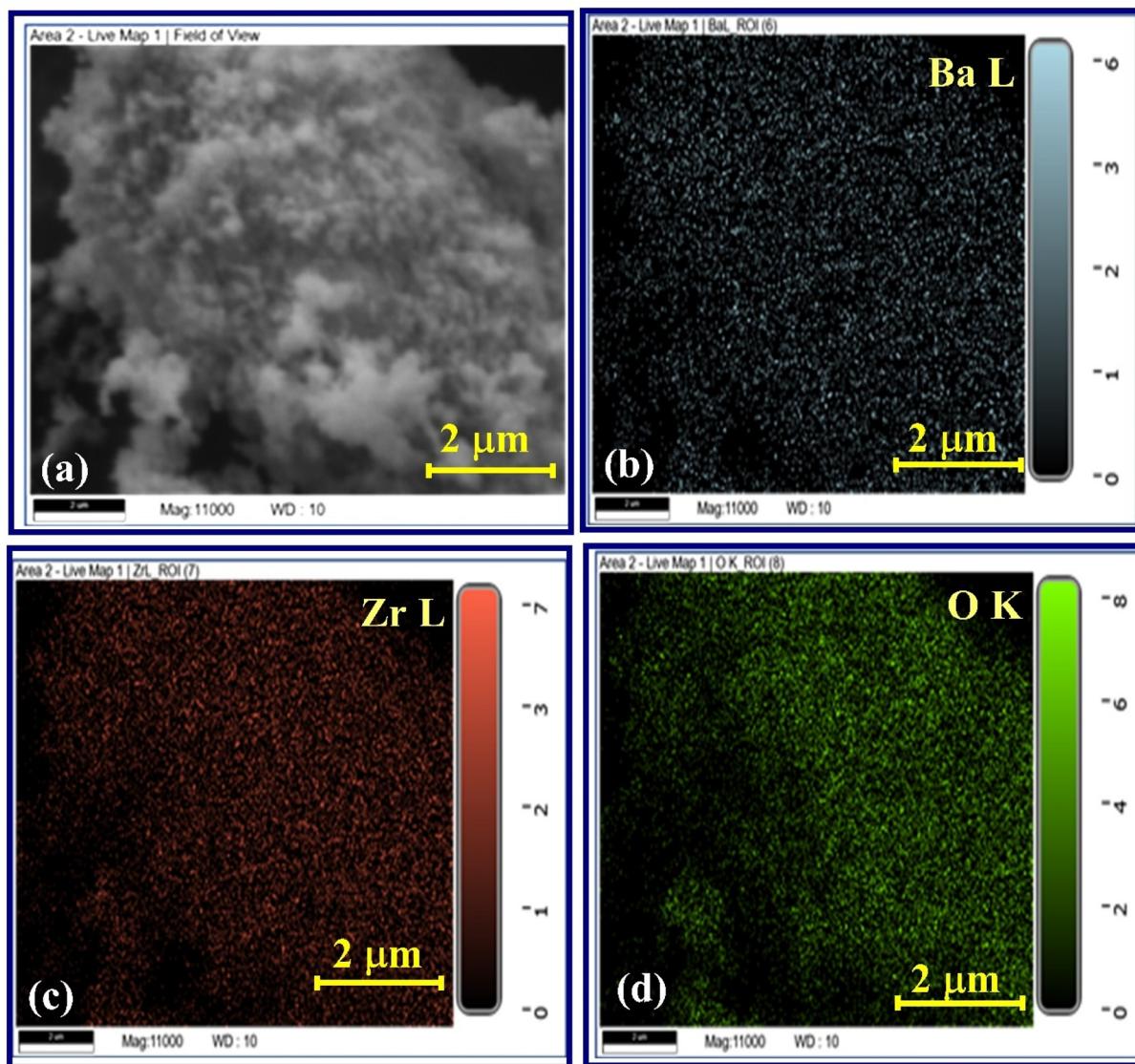
Fig. 5 (a) Field of view for EDS mapping, (b) EDS mapping for Ba L, (c) EDS mapping for Zr L and (d) EDS mapping of O K elements of BaZrO₃ nanoparticles.

pressure, as evidenced by the previously documented pressure-induced phase transition in BaZrO₃ crystals.[42–44]

Regarding lattice dynamics, this phase transformation corresponds to lattice instability at the Brillouin zone boundary points. The lattice instability identified in the present calculations aligns closely with earlier studies that employed a similar approach.

3.1.4 Vibrational spectroscopy analysis. FTIR spectroscopy is an effective analytical technique that can help to analyze the vibrational modes of molecules in a sample. By measuring the absorption of infrared radiation by the sample, we can gain valuable insights into its chemical composition and molecular structure. The FTIR spectra of BaZrO₃, as shown in Fig. 6(a), were acquired using a PerkinElmer FTIR spectrophotometer in the wavelength range of 4000 to 400 cm⁻¹. We have identified several prominent bands in the spectrum, situated at approxi-

mately 527, 615, 692, 857, 1059, 1455, 1754, 2452, and 3456 cm⁻¹. According to the existing literature, the infrared bands within the range of 400–750 cm⁻¹ correspond to metal–oxygen stretching vibrations at the B-site of the ABO_3 perovskite.[45,46] Additionally, a robust band detected at 572 cm⁻¹ represents the antisymmetric stretch of ZrO_6 clusters in the cubic BaZrO₃ perovskite ceramic.[30,47,48] At approximately 615 cm⁻¹ and 692 cm⁻¹, two bands are observed, each revealing distinct characteristics. The band at 615 cm⁻¹ corresponds to the Ba–O stretching vibrational mode, which signifies the features of the tetrahedral BaO_{12} groups present in the compound.[49] On the other hand, the band at 692 cm⁻¹ indicates the formation of Ba–O bonds within the compound.[49] The peak observed at 857 cm⁻¹ is attributed to the asymmetric vibration modes of NO_3^{-1} ions.[49] The band observed at approximately 1059 cm⁻¹ is linked to the O–O stretching
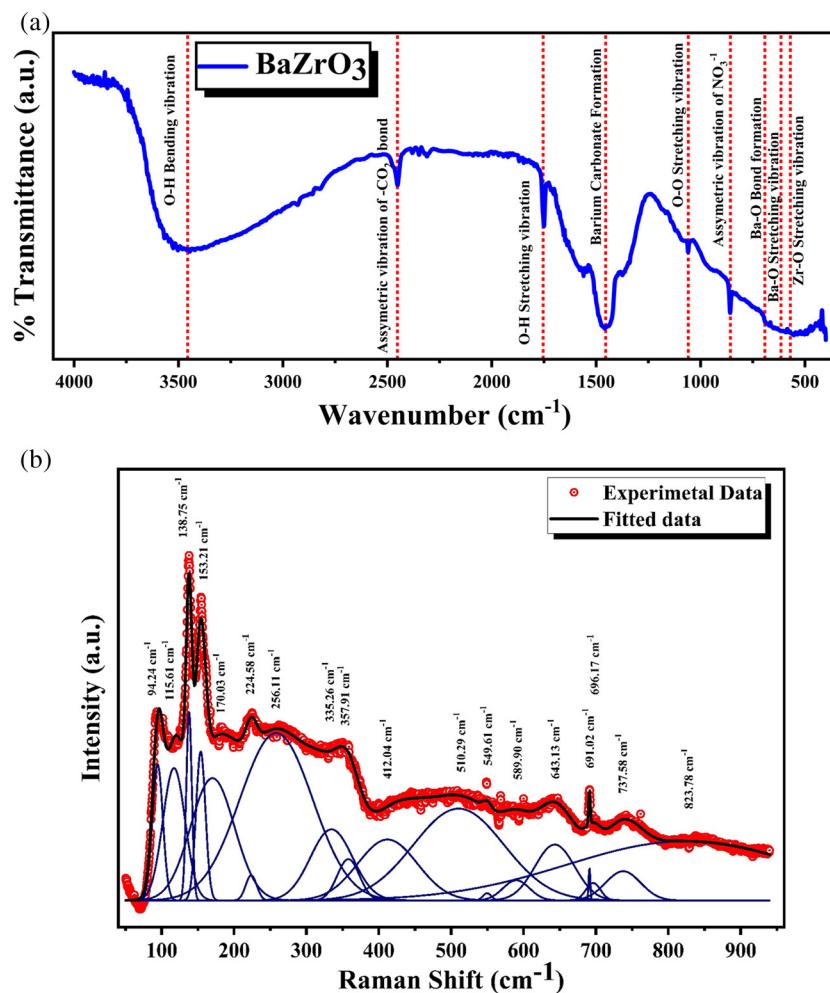
Fig. 6 (a) FT-IR spectra of $BaZrO_3$. (b). Room temperature Raman spectra of $BaZrO_3$ nanoparticles.

modes of vibration.[50] The band detected at 1447 cm^{-1} corresponds to the stretching band of $-CO_3^{2-}$ ions, indicating the formation of barium carbonate ($BaCO_3$).[47,51,52] This formation occurs due to the absorption of atmospheric CO_2 by $BaZrO_3$ nanoparticles. There are three absorption bands observed at approximately 1754, 2452, and 3456 cm^{-1}, each associated with specific vibrational modes. The band at 1754 cm^{-1} corresponds to the O–H stretching vibrational mode, the band at 2452 cm^{-1} is linked to the asymmetric vibration of the $-CO_2$ bond, and the band at 3456 cm^{-1} is connected with the O–H bending vibrational mode.[53,54] The FTIR spectra of the synthesized $BaZrO_3$-NPs reveal that no other absorption bands associated with any other chemical group have been found. This absence of additional bands indicates the high purity of the sample.

Raman spectroscopy stands as a remarkably sensitive and robust technique to investigate crystal structures through the analysis of their vibrational bands. By employing group theory analysis, one can ascertain the count of allowed vibrational modes in a specific crystal system. The factor group analysis for pertinent space groups is presented in Table 3.

Group theoretical studies suggest that perovskite materials with a pure cubic crystal structure do not exhibit first-order Raman active phonon modes in vibrational spectra at room temperature, resulting in the absence of a Raman spectrum.[55] However, experimental studies on $BaZrO_3$ samples contradict this, revealing the presence of some Raman active modes or bands (Fig. 6(b)). The literature provides two explanations for the Raman spectrum of simple cubic perovskites. The primary explanation involves second-order scattering, where two phonons with opposite parallel wave vectors undergo allowed transitions, resulting in a low-intensity peak. The less supported explanation attributes the spectrum to the breaking of local symmetry caused by tilt and structural disorder, allowing deviation from the selection rule, and producing active modes in Raman.[56] The local symmetry of barium zirconate is influenced by octahedral tilt, oxygen octahedral distortion, or structural instability. Therefore, the observed peaks in $BaZrO_3$ are likely a result of second-order scattering.[57,58]

Raman active modes are further categorized into two optical components: longitudinal (LO) and transverse (TO).

Table 3 The irreducible representations of the normal modes of vibrations of the BaZrO$_3$ ceramic at the zone center for the $Pm3m$ space group and $O_h{}^1$ point group with the corresponding site symmetry

Atoms	Site	Symmetry	X	Y	Z	Site species	Irreducible representation
						$Pm\bar{3}m$ space group ($O_h{}^1$)	
Ba^{2+}	1b	O_h	0.5	0.5	0.5	F_{1u}	F_{1u}
Zr^{4+}	1a	O_h	0.0	0.0	0.0	F_{1u}	F_{1u}
O^{2-}	3d	D_{4h}	0.5	0.0	0.0	A_{2u}	F_{1u}
						E_u	$F_{1u} + F_{2u}$

$\Gamma_{\text{Total}} = 4F_{1u} + F_{2u}$

No Raman active modes

$\Gamma_{\text{Acaustic}} = F_{2u}$

$\Gamma_{\text{IR}} = 4F_{1u}$

However, in the case of BaZrO$_3$, a perovskite that maintains its cubic phase across all temperatures, it also lacks first-order Raman active modes due to its symmetry constraints. Nevertheless, it exhibits a remarkably intense Raman spectrum, characterized by distinct and well-defined features. This intriguing spectral behavior is likely due to its second-order nature.[59] Fig. 6(b) depicts the room temperature Raman spectra of the BaZrO$_3$ ceramic. The spectra exhibit a comparable signature, bearing resemblance in their main features to the few spectra reported in the literature.[55,56,60–62] The three polar modes in cubic perovskites are commonly referred to as the "Slater" mode, involving an anti-phase motion of the B cation concerning the oxygen octahedra, the "Axe" mode, which entails an anti-phase motion of the apical oxygens with respect to the other oxygen atoms within the octahedra, and the "Last" mode, characterized by an anti-phase motion of the A cation and the ZrO6 octahedra.[63] These labels hold particular significance in the context of ferroelectric transitions.[63]

The Raman spectra of BaZrO$_3$ exhibit distinct bands at approximately 138.75, 357.91, and 691.02 cm^{-1}, which can be attributed to different zone center modes. Specifically, the 138.75 cm^{-1} band corresponds to the last mode, representing the displacement of Ba relative to the ZrO$_6$ octahedra.[64] The 357.91 cm^{-1} band corresponds to the Slater mode, signifying out-of-plane displacements of Zr in relation to in-plane oxygen atoms. Finally, the 691.02 cm^{-1} band corresponds to the Axe mode, indicating the displacement of apical oxygens with respect to in-plane oxygens. Additionally, the Raman mode observed at 94.24 cm^{-1} is associated with the anti-parallel motion of Ba–O. Two first order transverse optical Raman modes, TO$_2$ and TO$_4$ are observed at 170.03 and 549.61 cm^{-1}. Second-order modes are identified at frequencies of approximately 224.58, 412.04 and 589.90 cm^{-1}. Furthermore, three bands are observed at approximately 115.61, 224.58, and 510.29 cm^{-1}, all representing f$_{1u}$ modes. The band at 153 cm^{-1} aligns with the presence of BaCO$_3$, which may also leave a distinctive mark in XRD analysis. However, we would like to emphasize that the presence of BaCO$_3$ is expected in our synthesis process, and its contribution to the spectra is consistent with its known presence as a precursor. This observation aligns well with previously reported data.[55] The mode at 115.61 cm^{-1} is associated with cation-ZrO$_3$ lattice vibrations, while the mode at 224.58 cm^{-1} corresponds to O–Zr–O bending vibrations and the mode at 510.29 cm^{-1} represents

Zr–O stretching vibrations. Notably, the last two modes (224.58 and 510.29 cm^{-1}) are independent of the Ba cation. Additionally, the vibrational modes observed at approximately 696.17 cm^{-1} are associated with distortions occurring at the octahedral site of zirconium within the BaZrO$_3$ unit cell.[55–64]

3.1.5 XPS analysis. X-ray photoelectron spectroscopy (XPS) was utilized in the binding energy range from 1200 eV to 0 eV to analyze and determine the surface chemical compositions and oxidation states of the BaZrO$_3$ ceramic. Fig. 7 presents a graphical representation of both the survey spectrum and the associated binding energy spectra for the Ba 3d, Zr 3d, and O 1s states within the BaZrO$_3$ compound and all the XPS parameters are listed in Table 4. The survey spectrum depicted in Fig. 7(a), illustrates that the as-prepared BaZrO$_3$ ceramic primarily comprises the elemental components Ba, Zr, and O, signifying the formation of a phase-pure BaZrO$_3$ ceramic. Furthermore, the confirmation of the precise valence state of each constituent element was achieved through its corresponding high-resolution (HR) scan. In Fig. 7(b), the HR-XPS spectrum for BaZrO$_3$ displays two well-defined peaks within the Ba 3d orbital, with energy levels recorded at 778.9 eV and 794.0 eV, corresponding to the spin–orbit splitting components of Ba 3d$_{5/2}$ and Ba 3d$_{3/2}$ core levels, respectively.[65,66] The binding energy difference between these two Ba 3d peaks (i.e. $\Delta E_{\text{BE}} = \text{BE}_{3d_{3/2}} - \text{BE}_{3d_{5/2}} = 15.1$ eV) aligns well with previous reports, affirming the presence of Ba ions in a 2+ valence state in the synthesized ceramic.[67] Additional peaks observed at 782.609 and 795.519 eV are attributed to oxidized surface species of barium, while the peak at 805.009 eV indicates negligible barium loss during synthesis.[67,68] Since barium exists in the Ba^{2+} oxidation state in both BaCO$_3$ and BaZrO$_3$, both compounds exhibit Ba 3d$_{5/2}$ signals at approximately 779.4 eV.[69] In our study, the Ba 3d orbital energy levels were recorded at 778.9 eV for Ba 3d$_{5/2}$. Thus, the separate signal for the presence of BaCO$_3$ in BaZrO$_3$ is not distinctly observed in the present XPS spectra.

In Fig. 7(c), the HR-XPS spectrum for the Zr 3d orbital is presented. The Zr 3d peaks can be primarily deconvoluted into two components: those around 177.542 eV correspond to Zr 3d$_{5/2}$, and those at approximately 181.361 eV are attributed to Zr 3d$_{3/2}$, indicating Zr^{4+} oxidation states, consistent with the existing literature.[68] The observed spin–orbit splitting, i.e., the difference between the binding energy of Zr 3d$_{3/2}$ and Zr 3d$_{5/2}$, doublets, (i.e. $\Delta E_{\text{BE}} = \text{BE}_{3d_{3/2}} - \text{BE}_{3d_{5/2}}$) measures 3.819 eV,
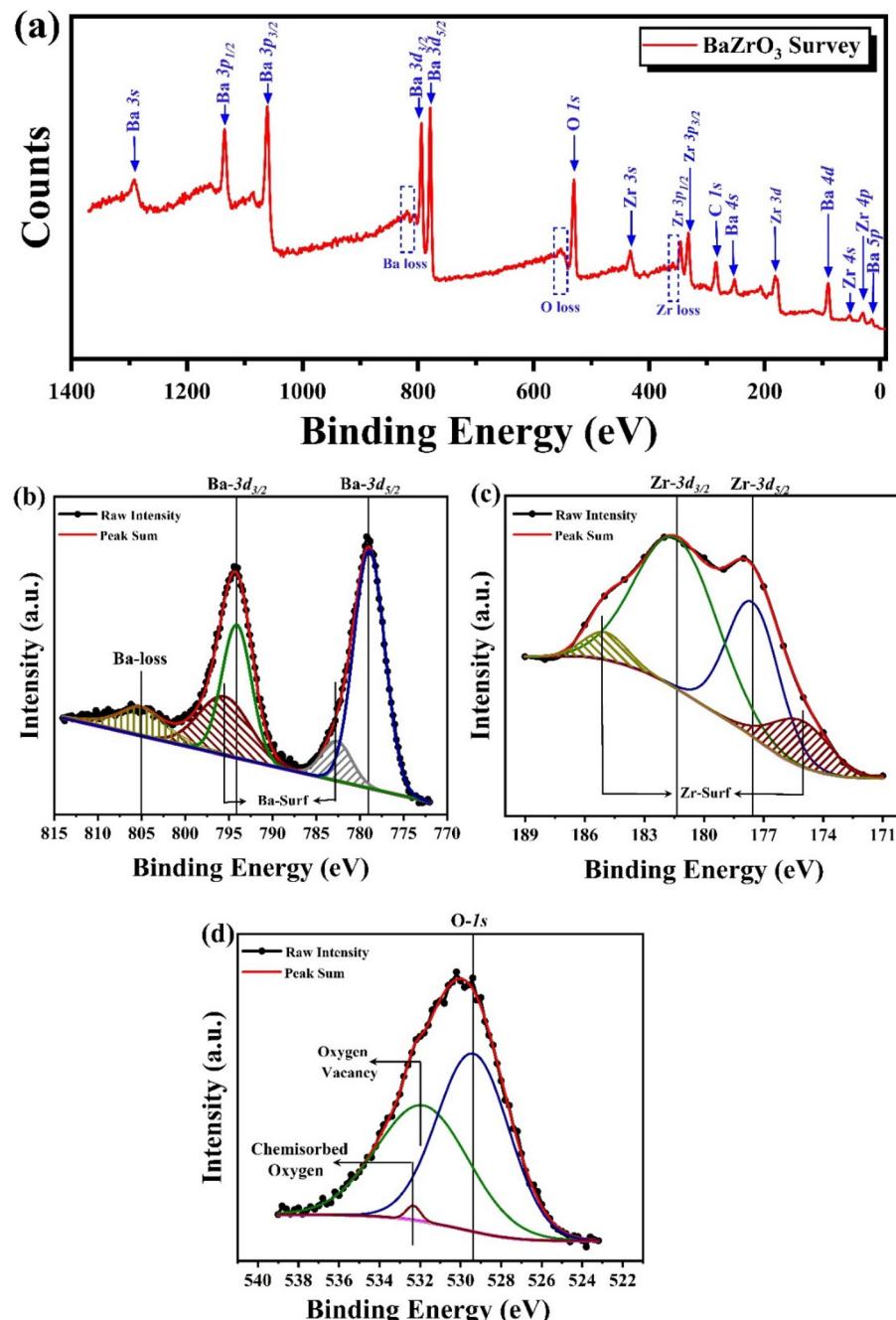
Fig. 7 (a) XPS survey spectra of BaZrO$_3$ nanoparticles (b) XPS spectra of Ba-3d element, (c) XPS spectra of Zr-3d element, and (d) XPS spectra of O-1s element.

aligning with previous findings.[70] The presence of spin–orbit split components in the core-level spectra of Ba 3d and Zr 3d, with separations of 15.193 and 3.819 eV, respectively, confirms the +2 and +4 oxidation states of Ba and Zr in the BaZrO$_3$ ceramic.[71,72] Peaks observed at 175.110 and 184.984 eV are attributed to oxidized surface species of zirconium.[67]

Fig. 7(d) presents the high-resolution XPS spectra of oxygen 1s. For pristine BaZrO$_3$, the spectra can be deconvoluted into three peaks at 529.374, 531.850, and 532.330 eV, respectively.[73] The characteristic peak of lattice oxygen is evident in the O 1s core-level spectra at 529.374 eV,[63] while the peak at 531.850 eV is possibly associated with oxygen vacancies,[74] and the peak at 532.330 eV arises due to surface hydroxyl groups.[75]

3.2 Ferroelectric PE loop

Polarization *versus* electric field (P–E) hysteresis loops were employed for the examination of the ferroelectric characteristics of BaZrO$_3$ ceramics. Fig. S4† presents the P–E hysteresis curves for the BaZrO$_3$ ceramic at room temperature, measured at a frequency of 50 Hz. These curves demonstrate a distinctive

Table 4 XPS parameters of the BaZrO₃ ceramic

Atom	Orbital	Binding energy	FWHM	Area	Peak specification
Ba^{2+}	3d	778.902	4.207	47 138.09	$3d_{5/2}$
		782.628	4.074	7550.826	Surface
		794.083	3.912	23 517.36	$3d_{3/2}$
		795.418	6.845	21 014.05	Surface
		805.093	6.866	7622.065	Ba-Loss
Zr^{4+}	3p	175.11	3.14	1703.944	Surface
		177.54	3.06	4602.614	$3d_{5/2}$
		181.36	4.85	7983.784	$3d_{3/2}$
		184.98	2.15	773.7342	Surface
O^{2-}	1s	529.374	4.174	19 391.94	Lattice oxygen
		531.850	5.306	16 481.81	O_2^- vacancy
		532.330	0.792	306.157	Chemisorbed oxygen

saturated loop to a certain extent, as evidenced by the presence of leakage within the P–E hysteresis loop. This behavior can be attributed to the presence of pinning defects and the accumulation of free charges at both the grain and grain boundaries.[31] The magnitude of ferroelectric parameters, such as remanent polarization and coercive field, is derived from the P–E loop. Notably, they exhibit a remanent polarization (P_r) of 0.068 μC cm^{-2}, saturation polarization (P_s) of 0.11789 μC cm^{-2} and a coercive field (E_c) of 9.39 kV cm^{-1}.

The squareness of the ferroelectric ceramic can be determined utilizing the Haertling and Zimmer correlation.

$$R_{sq} = \frac{P_r}{P_s} + \frac{P_{1.1Ec}}{P_r} \tag{3}$$

In this context, R_{sq} represents the squareness parameter of the hysteresis loop. P_r denotes the remanent polarization, P_s indicates the saturated polarization at a finite field strength below dielectric breakdown, and $P_{1.1Ec}$ stands for the polarization at a field equal to 1.1Ec. According to the literature, the ideal square loop (R_{sq}) of a ceramic equals 2.00. For BaZrO₃, the estimated R_{sq} value is approximately 1.80.

3.3 UV-Vis spectroscopy analysis

The bandgap of a semiconductor, a critical parameter in materials science, signifies the energy difference between its valence and conduction bands, determining its electrical conductivity characteristics. A narrower bandgap denotes a better conductor and researchers harness specific bandgap values to tailor semiconductor materials for precise electronic applications like diodes and transistors. Moreover, the bandgap significantly influences a semiconductor's thermal properties, impacting its efficiency in thermoelectric devices used for heat-to-electricity conversion, making it a pivotal factor in materials selection and device design.

In recent research, the optical properties of BaZrO₃ have garnered considerable attention due to its optical band gap, which has been determined to be approximately 4.8 eV using UV-visible spectroscopy.[70,71,73] The optical band gap serves as a critical parameter denoting the energy threshold required for photons to be absorbed by the material. It is noteworthy that this optical band gap tends to be somewhat narrower than the

corresponding electrical band gap, a characteristic observed in various perovskite oxide materials. This unique feature has stimulated the exploration of BaZrO₃'s potential in a range of optical applications, particularly in the visible and ultraviolet (UV) spectral regions. The material's substantial band gap, which falls within the range of 3.8 to 7.0 eV, underscores its versatility and suitability for diverse photon-based technologies, making it an attractive candidate for future optoelectronic and photonic devices.[15,30,76]

The efficiency of a photocatalyst relies significantly on its light absorption capability, crucial for initiating photogenerated charge carriers within the material. Fig. 8(a), describes the absorbance (A) *versus* the wavelength (λ) of BaZrO₃ in three radiation domains: UV (ultra-violet), Vis (visible) and NIR (near infrared). The absorption band is observed in the UV-region in the wavelength range of 200–800 nm.

Fig. 8(a) illustrates that BaZrO₃ exhibits its primary absorption peak at 230 nm, attributed to band-to-band transition. Additionally, a band tail extending beyond 400 nm is evident, indicating the presence of disordered states, defect states, or oxygen vacancies within the compound. Such impurities or defect-state transitions typically manifest as band tails in semiconductor absorption spectra.[6] The occurrence of absorption
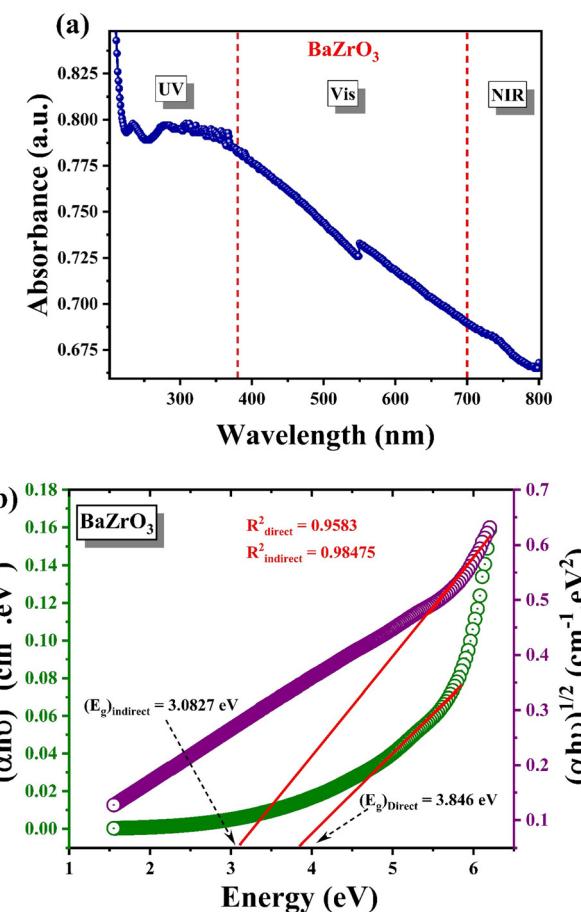
Fig. 8 (a) UV-Vis spectra of BaZrO₃. (b) Tauc plot of BaZrO₃ nanoparticles.

bands in the UV-VIS range indicates the capability of $BaZrO_3$ to absorb UV and visible light. This characteristic renders them suitable for applications such as UV-VIS light absorption, the development of photovoltaic solar cells, and the creation of photocatalytic materials.[77] Semiconductors in photovoltaic solar cells can capture energy from both UV and visible light, enabling the generation of electricity. In photocatalysis, these semiconductors can also promote chemical reactions upon exposure to either UV or visible light.[78] The absorbance-wavelength spectra enabled the determination of an optical bandgap energy value that corresponds to the absorption band observed in the UV-Vis region. The determination of the bandgap energy for the $BaZrO_3$ sample under study can be accomplished using Tauc's law[31,32]

$$\alpha h\nu = \beta(h\nu - E_g)^n \tag{4}$$

In this equation, '$h\nu$' represents the photon energy of the substance and 'β' is a constant. In this particular scenario, two distinct optical transitions were identified: one with 'n' equal to 1/2, indicative of a direct transition type, and another with 'n' equal to 2, signifying an indirect transition. The determination of the band gap energy can be accomplished by applying the Tauc expression provided below.

$$(\alpha h\nu)^{1/n} = \beta(h\nu - E_g) \tag{5}$$

Fig. 8(b) illustrates the plots of $(\alpha h\nu)^{1/2}$ and $(\alpha h\nu)^2$ as a function of varying photon energy ($h\nu$) for the $BaZrO_3$ compound. By linearly extrapolating the curves shown in Fig. 8(b) to zero $h\nu$, the determined values for the indirect and direct band gap energies are found to be $(E_g)_{indirect}$ = 3.0827 eV and $(E_g)_{Direct}$ = 3.846 eV, respectively. The observed band gap energy (E_g) for the sample produced in this study is lower than that reported in previous research. This reduction in the band gap is attributed to the high sintering temperature and is indicative of the quantum confinement effect.[79] Moreover, upon comparing our findings with theoretical values, we find a good match, confirming that the band gap energy has indeed decreased. Reducing the bandgap value can boost the rate of electron–hole pair generation on the surface of the nanocatalyst, leading to an overall improvement in photocatalytic activity.[21,22]

The determination of the refractive index in $BaZrO_3$ is accomplished using a contemporary empirical linear relationship between the energy band gap and refractive index, as proposed by Paswan[80] et al.

$$n = 4.084 - 0.62E_g \tag{6}$$

Subsequently, Fresnel's equation is utilized to compute the corresponding reflectance value.

$$R = \frac{(n-1)^2}{(n+1)^2} \tag{7}$$

The determined value for 'n' in the case of $BaZrO_3$ is 2.17, while the computed value for 'R' stands at 0.1375.

3.4 Photocatalytic degradation

Maximizing the semiconductor's absorption of incident sunlight stands as a powerful method to elevate the catalytic prowess of a photocatalytic material.[81,82] Under consistent reaction parameters, the efficacy of a $BaZrO_3$ catalyst was examined in conjunction with an initial RhB concentration set at 10 mg L^{-1} (10ppm). During experimentation, it was observed that elevating the initial dye concentration up to an optimal threshold corresponded to an escalation in RhB degradation. Nevertheless, exceeding this optimal concentration resulted in a decline in RhB degradation. Boczkaj et al. reported the highest degradation of RhB, reaching 37.3%, which occurred at an initial concentration of 10 ppm, while the lowest degradation, at 16%, was recorded at a concentration of 6 ppm.[83] Arti et al.[84] investigated the photocatalytic behavior of Dy^{3+}-doped $BaZrO_3$ nanopowders, highlighting significant enhancements in photocatalytic, photoluminescence, and fingerprint properties. Their findings revealed that optimal degradation was achieved within the first 180 minutes, after which no further degradation was observed. The kinetic analysis indicated that the degradation process followed zero-order kinetics, with a rate constant of 0.015 and an R^2 value of 0.98, suggesting a strong correlation with the prepared nanopowder. In a related study, Jana et al. conducted an in-depth exploration of doped double perovskites, such as $K_2Ta_2O_6$ and Ba_2TiMoO_6, uncovering their potential to significantly enhance the photocatalytic degradation rates of pollutants like methylene blue. The study elucidated the critical role of hydroxyl radicals as the primary reactive species driving these degradation processes.[85] As per the literature survey, Yi et al.[102] also observed analogous findings, noting a rise in the degradation rate from 0.00117 to 0.00136 min^{-1} with variations in the initial RhB concentration, ranging from 20 to 40 μmol L^{-1}. This reveals that the extent of degradation depends on the generation of hydroxyl radicals and the accessibility of contaminants for reaction. Consequently, the role played by the initial concentration of the RhB dye emerges as a critical parameter for optimizing degradation processes. The previous literature presents a compilation of results concerning the application of $BaZrO_3$ with diverse dyes, systematically recorded in a table format. Table 5 outlines the overall degradation efficiency of different industrial dyes using the $BaZrO_3$ catalyst.

The photocatalytic activity of the synthesized catalyst was examined by assessing its ability to degrade rhodamine B under visible light irradiation (λ = 400 nm) using a 150 W Xe lamp. Under visible light irradiation, the color of the RhB/$BaZrO_3$ suspension changes and the absorption gradually decreases, indicating that the ethyl groups were removed and thus, RhB was degraded. When exposed to visible light, $BaZrO_3$ becomes activated and generates photo-induced electron–hole (e^-/h^+) pairs. Following this, photo-induced electrons rapidly migrate from $BaZrO_3$ to RhB. As a widely recognized phenomenon, these photo-induced electrons efficiently catalyze the reduction of O_2 molecules adsorbed on the surface of RhB/$BaZrO_3$, yielding O_2^{*-} radicals that play a

Table 5 Comparative photocatalytic properties from our results and those in some published studies

S. No.	Photocatalyst	Illumination	Synthesis method	Contaminant	Results	Ref.
1.	BaZrO$_3$	UV radiation	Green synthesis	CR dye	Degradation efficiency, 84.1% in 90 min, k = 0.0175 min^{-1}	Kayathiri et al., (2022)[9]
2.	BaZrO$_3$:W 15%	UV–A	Hydrothermal synthesis	Levofloxacin	Degradation efficiency 93.4% and k = 1.27 × 10^{-2} min^{-1}	Gulen et al. (2021)[64]
3.	BaZrO$_3$:W 5%	Visible light	Hydrothermal synthesis	Tetracycline	Degradation efficiency 94.9% and k = 1.01 × 10^{-2} min^{-1}	Gulen et al. (2021)[64]
4.	BaZrO$_3$:Dy^{3+}	UV illumination	Hydrothermal synthesis	Methylene Blue	Degradation efficiency 78.66%, in 180 min and k = 0.015 min^{-1}	Aarti et al. (2024)[84]
5.	3% carbon dots modified BaZrO$_3$	UV radiation	Facile carbonation process via the hydrothermal route	Methylene Blue	Degradation efficiency ~90%	Patra et al. (2018)[6]

pivotal role as key active species in the degradation process.[86] In addition, the photo-induced h$^+$ can oxidize RhB or react with H$_2$O to generate OH* radicals. The generated OH$^•$ and O$_2^{*-}$ radicals can then oxidize RhB. The photo-degradation mechanism of RhB by BaZrO$_3$ can be described by the following reactions:[87]

$$BaZrO_3 + h\nu \rightarrow e_{CB}{}^-(BaZrO_3) + h^+{}_{VB}(BaZrO_3) \quad (8)$$

$$h^+{}_{VB}(BaZrO_3) + H_2O \rightarrow OH* + H^+ \quad (9)$$

$$e_{CB}{}^-(BaZrO_3) + O_2 \rightarrow O_2^{*-} \quad (10)$$

$$h_{VB}{}^+(BaZrO_3) + RhB \rightarrow Degradation\,Products \rightarrow CO_2 + H_2O \quad (11)$$

$$O_2^{*-} + RhB \rightarrow Degradation\,Products \rightarrow CO_2 + H_2O \quad (12)$$

$$OH* + RhB \rightarrow Degradation\,Products \rightarrow CO_2 + H_2O \quad (13)$$

$$h^+ + e^- \rightarrow (e^-, h^+)\,(negligible\,recombination) \quad (14)$$
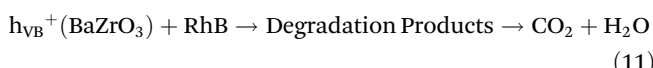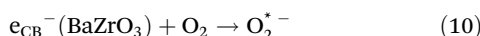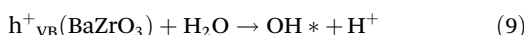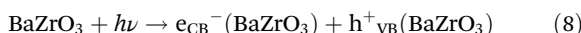
Fig. 9(a) displays the temporal UV-vis spectral changes of RhB aqueous solution during photocatalytic degradation reactions. Under visible light irradiation (λ = 400 nm) in the presence of BaZrO$_3$, the primary absorbance peaking at 552 nm significantly decreased with irradiation time, resulting in approximately 35 to 38% degradation after 40 minutes of irradiation, as depicted in Fig. 9(a). The efficiencies of the photocatalytic degradation under visible light irradiation are illustrated in Fig. 9(b), where C represents the absorption of
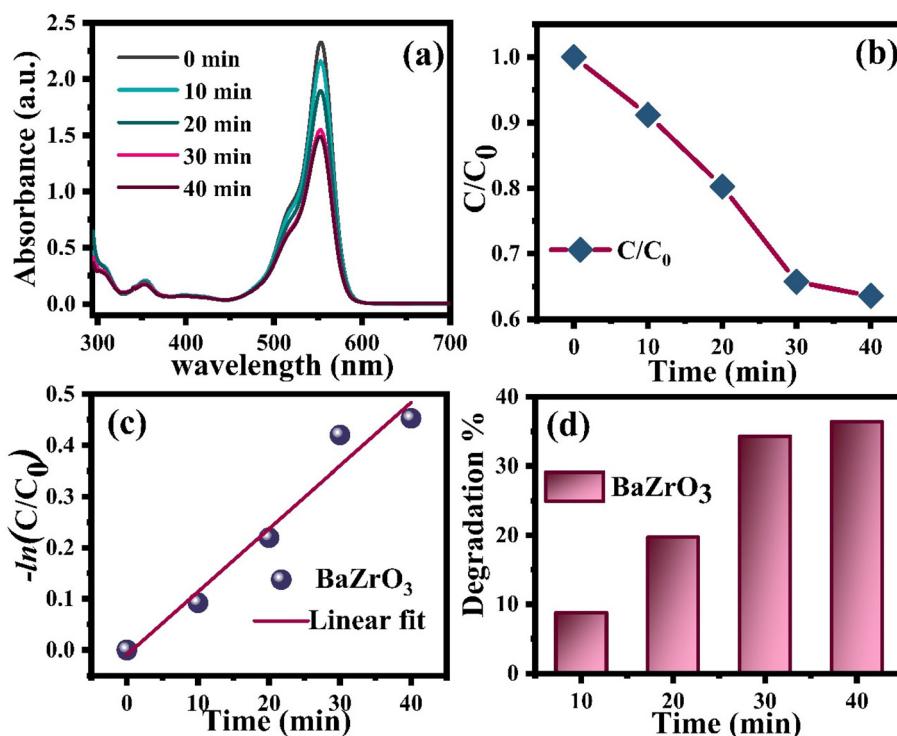

Fig. 9 (a) Degradation absorbance spectra of RhB dye using BaZrO$_3$ nanoparticles, and (b) and (c) degradation rate. (d) Efficiency of dye for degradation under visible light.

RhB at a wavelength of 552 nm, and C_0 signifies the absorption after adsorption equilibrium on $BaZrO_3$ before irradiation.

The $BaZrO_3$ photocatalyst undergoes energy absorption upon illumination with light. Upon reaching or surpassing the energy band-gap of $BaZrO_3$, the transfer of electrons (e^-) occurs from the valence band to the conduction band. The transitions lead to the creation of holes (h^+) in the valence band, and the resulting electron–hole pairs (e^- and h^+) generated by the photo-excitation process then migrate towards the surface of $BaZrO_3$. However, the energy transfer induced by the photo-excitation is directed towards the adsorbed species, where the electrons are responsible for reducing the oxygen (O_2) molecule to the oxygen-radicals (O_2^{*-}), which are further converted into hydroxyl-radicals ($OH^\star$). Meanwhile, the holes produced by the photo-excitation process oxidize the hydroxyl (H_2O) molecule to generate the hydroxyl-radicals ($OH^\star$).[88] The resulting hydroxyl-radicals ($OH^\star$) are effective at decomposing RhB. The value of k is reported to be ~0.0123 min^{-1}, as shown in Fig. 9(c). The degradation efficiency of $BaZrO_3$ reached ~36.41% when exposed to UV-Visible light for a duration of ~40 minutes, as recorded in Fig. 9(d).

3.5 DFT analysis

3.5.1 Electronic band structure. The electronic band structure of the $BaZrO_3$ ceramic was calculated using PBE-GGA exchange correlation function along with the high-symmetry Brillouin zone points $\Gamma \rightarrow R \rightarrow X \rightarrow M \rightarrow \Gamma$ in the energy range of −5 to 8 eV. Fermi level is the level which occurs at 0.0 eV energy below which all energy states are occupied and above all are unoccupied. The indirect energy band gap from R → X BZ points is found to be 3.0497 eV which is consistent with the values reported in the literature. The top of the conduction band lies on the R point and the bottom of the valence band lies on the X point, indicating the origin of the indirect band gap in the $BaZrO_3$ semiconducting ceramic.[16,20,75,89,90] The optical band edge originated from the electronic transition between O 2p/Zr 4p and Ba 4d orbitals. While the direct band gap at $\Gamma \rightarrow \Gamma$ is 3.325 eV.

From Fig. 10(a), it is seen that the minimum conduction band of $BaZrO_3$ mainly consists of the Zr 4d orbital and a minor hybridization of Ba 4d orbital in the energy region from 4 to 6 eV. The maximum valence band consists of the hybridization of O 2p and Zr 4p orbitals in the energy region from −0.2044 eV to −4.0680 eV. Indeed, the s and p states of the zirconium atom, as well as the s state of the barium atom, exert a partial influence on these valence bands, and their presence can be observed. At energy levels surpassing the Fermi energy, which corresponds to the conduction band, there exist vacant states, including the unoccupied 4d states of the zirconium atom and the 6s and 5d states of the barium atom.[91,92]

3.5.2 Density of states. The distribution of electrons in a particular energy range can be demonstrated with the help of DOS. The elemental density of states (DOS) of $BaZrO_3$ is shown in Fig. 10(b), using PBE-GGA, consistent with the band structure diagrams obtained with the same functional. The Fermi energy level is set at 0 eV. $BaZrO_3$ exhibits semiconductor characteristics with a bandgap (E_g) of 3.05 eV. This calculated bandgap aligns well with previous theoretical data but is underestimated compared to the experimentally measured bandgap from the UV-Vis spectrum.[89–93] Such underestimation of bandgap values is a common feature observed in various perovskite oxide materials and different exchange–correlation functionals in DFT calculations. Specifically, Rizwan *et al.* reported an indirect bandgap of approximately 3.127 eV from the R to Γ symmetry point using PBE-GGA in the CASTEP code.[94] Zeba *et al.* found a similar value of 3.119 eV from the R to Γ point.[75] Erum *et al.* investigated the indirect bandgap of $BaZrO_3$ using different exchange–correlation functionals and found that the value obtained using PBE-GGA from the Γ to M symmetry point is 3.273 eV.[95] Additionally, Lopez-Candales *et al.* studied the bandgap of cubic $BaZrO_3$ using PBE-GGA and reported an indirect bandgap from the R to Γ Brillouin Zone point of 3.23 eV, with a direct bandgap at the Γ point being 3.44 eV.[96] Zulfiqar *et al.* provided a value of 3.22 eV for the electronic bandgap using PBE-GGA.[97] Our calculated bandgap value using the electronic band structure with the PBE-GGA exchange–correlation functional aligns well with these previously reported studies.

The symmetrical pattern of density of the states indicates the existence of non-magnetism in $BaZrO_3$. As shown in
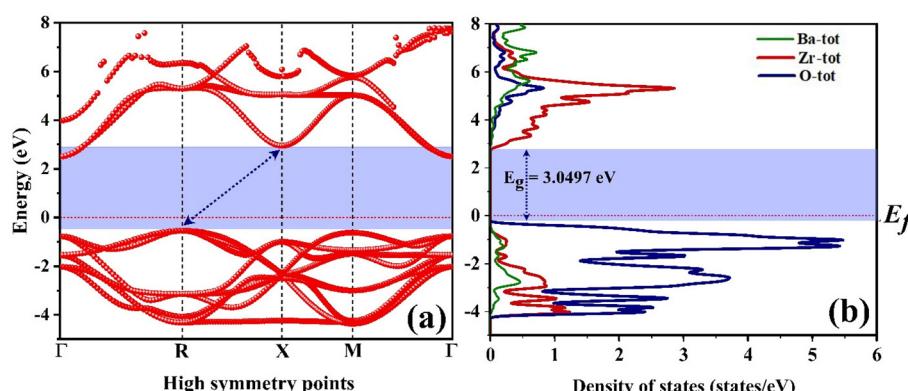
Fig. 10 (a) Electronic band structure, (b) total density of states of $BaZrO_3$ nanoparticle.

Fig. 10(b), the conduction band of $BaZrO_3$ is mainly composed of Zr 4d states while the valence band is strongly dominated by O 2p.

In order to investigate the contribution of various atomic orbitals (s, p, and d orbitals) of $BaZrO_3$, the projected density of states (PDOS) ranging from −5 eV below the top of the VB to 10 eV above the top of the VB band has been computed and illustrated in Fig. S5.† It represents the main orbital that influences the gap state. In the VB main role is played by O 2p (p_x, p_y, and p_z) orbitals within a range of −0.3 eV to −4.3 eV due to the admixture of Zr (4d) and Ba (5p, 6s) states just below the Fermi level, which can be seen in Fig. S5(a and b).† This is expected due to the large electronegativity of oxygen (3.44 eV) as compared to Ba (0.89 eV) and Zr (1.33) (Pauling scale). It is also to be noted that the formation of the conduction band maximum (CBM) is dominated by the d-orbital contribution of the Zr atoms except for a small contribution of the p-orbital of O atoms (especially p_z orbital). To explore further the orbital contribution to the conduction bands, PDOS for d-orbitals of Zr atoms have also been analyzed and are presented in Fig. S5(b).† The conduction band minima is mainly contributed by the d_{xz} orbital of Zr(4d) atom with minor contribution from d_{xy} and d_{yz} orbitals within the energy range from 2.86 to 8.17 eV.

3.5.3 Bader charge analysis. To perform a quantitative assessment of the bonding characteristics in the $BaZrO_3$ ceramic, we computed the effective Bader charges for the host cations and oxygen atoms based on electron density using the Bader method.[98–100] The resulting data are presented in Table 2. According to the Bader analysis, the effective charge on Ba is +1.5229 (equivalent to 76.145% of its nominal 2+ ionic charge), on Zr it is +2.49 (equivalent to 62.38% of its nominal 4+ ionic charge), and on O it is −1.3394 (equivalent to 66.97% of its nominal 2− ionic charge). These percentages are indicative of how close the effective charges are to their expected ionic values.

Significantly, our results are in agreement with previously reported data in the scientific literature.[101] The Bader analysis underscores a greater covalent nature in the Zr–O bonds as opposed to the Ba–O bonds. This observation becomes apparent when considering that the effective Bader charge of Ba represents 76.145% of its ionic threshold, while Zr's effective Bader charge falls significantly shorter at 62.38% of its ionic limit. Hence, the Bader analysis highlights that within $BaZrO_3$, the Zr–O bond demonstrates a reduced ionic quality and a heightened covalent aspect when compared to the Ba–O bond.

3.6 Photoluminescence spectroscopy analysis

In the context of $BaZrO_3$ nano-crystallites studied here, structural defects like the presence of Ba, Zr, and oxygen interstitials, as well as vacancies, give rise to a variety of radiative transitions. These transitions involve electrons located in either the conduction band or trapping levels interacting with holes situated in either the valence band or trapping levels.[31,35] For a more thorough comprehension of the emission phenomenon, photo-luminescence analysis stands as a frequently utilized
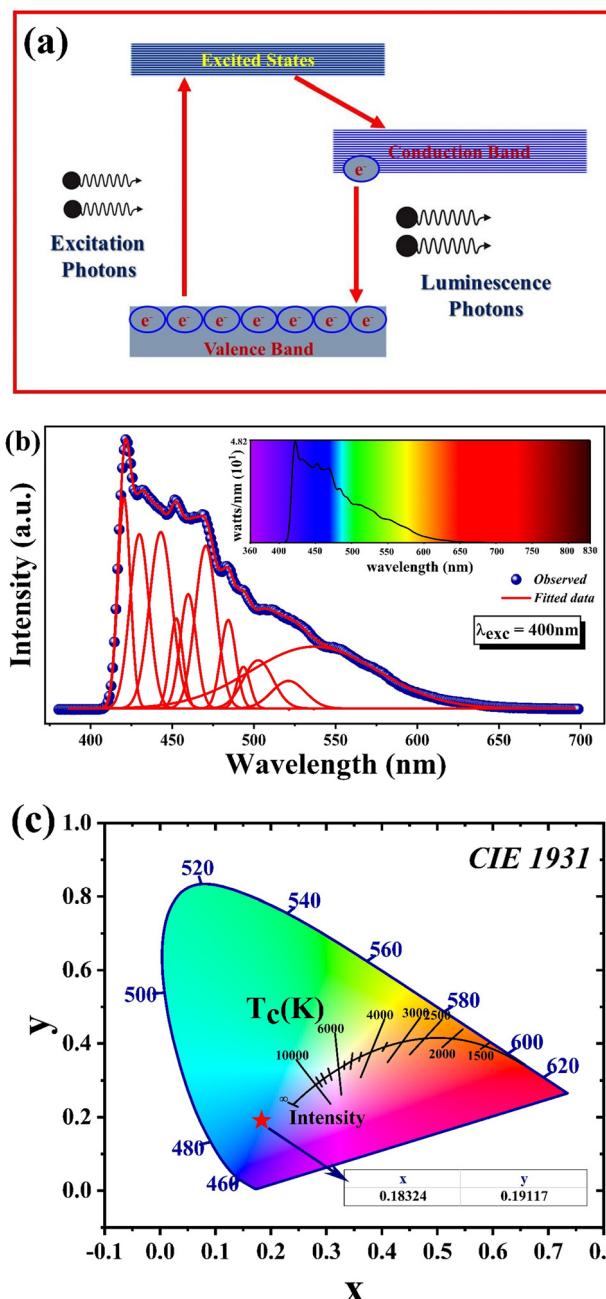
Fig. 11 (a) Photoluminescence mechanism. (b) Photo luminescence spectra at the excitation wavelength λ_{exc} = 400 nm. (c). CIE diagram of $BaZrO_3$ nanoparticles.

and indispensable investigative technique. Fig. 11(a) provides a schematic representation of the photoluminescence excitation.

The room temperature photoluminescence spectra of $BaZrO_3$ nanoparticles, synthesized through a straightforward one-step flash combustion method, employing an excitation wavelength of 400 nm is showcased in Fig. 11(b). When subjected to this 400 nm excitation, the spectra manifest a prominent and expansive range of violet-blue emissions. Specifically,

the violet emission peaks are located at 420.57 nm and 429.90 nm, while the indigo emission peaks are discernible at 442.98 nm, 452.49 nm and 459.82 nm and the blue emission peaks are discernible at 470.6 nm, 484.32 nm and 493.60 nm. The peaks at 502.63 nm, 521.17 nm and 536.96 nm correspond to the Green region.

The photoluminescence (PL) emission spectra depicted in Fig. 11(b) demonstrate a continuous spectrum of emissions, owing to the involvement of multiple components. To assess each component individually, it is imperative to deconvolute the spectra. Street and Bevingt proposed that these profiles could be separated using a Lorentzian line shape function. In our current study, we employed the Gaussian line shape function to deconvolute the PL spectra, effectively utilizing the Lorentzian line shape to fit the emission peaks. Emission peaks at 420.57 nm (2.94 eV), 429.90 nm (2.88 eV), 442.98 nm (2.79 eV), 452.49 nm (2.74 eV), 459.82 nm (2.69 eV), 470.60 nm (2.63 eV), 484.32 nm (2.56 eV), 493.60 (2.51 eV), 502.63 nm (521.17 eV) and 536.96 nm (2.30 eV) nm were observed. The presence of these emission bands signifies the existence of seven strong and distinct electronic transitions within the visible spectrum, spanning from violet to yellow wavelengths.[19,20] Nevertheless, it is worth noting that the most prominent emission peak, which appears at approximately 420.57 nm (equivalent to 2.94 eV), displays the highest intensity among all the observed emissions. This emission peak suggests that $BaZrO_3$ exhibits heightened activity in the violet light region when subjected to visible light irradiation.[90,91] The radiative defect peaks are observed at 420.57 and 429.90 nm. Size-dependent excitonic transition is responsible for the emission peak at 470.60 nm.[76] The peaks at 502.63, 521.17, and 536.96 nm might have been originated from vacancies or point defects which are either extrinsic or intrinsic that form recombination centers. The presence of recombination sites and defects can also play a role in influencing the process.[30,101]

The Commission International de I' Eclairage (CIE) chromaticity coordinates are crucial factors for evaluating the luminescence properties of phosphors.[31] The CIE 1931 x–y chromaticity diagram of $BaZrO_3$ nanophosphors were presented in Fig. 11(c). According to PL spectra, the CIE chromaticity coordinates (x, y) of $BaZrO_3$ are (0.18324, 0.19117). The red star in Fig. 11(c) represented the location of the CIE chromaticity coordinate of $BaZrO_3$ under excitation wavelength 400 nm. These coordinates are situated in the violet-blue region, indicating the dominant color of the emitted light, which further verifies the potential application of $BaZrO_3$ nanophosphors in the production of intense violet-bluish LEDs.

4. Conclusion

This study introduces a comprehensive investigation into refining the structural and electro-optical properties of $BaZrO_3$, a visible light-emitting photocatalyst. Using a single-step flash combustion method with glycine as the fuel, we synthesized $BaZrO_3$ nano-ceramics, confirmed in the cubic $Pm\bar{3}m$ (221) space group with a crystallite size of 70.29 nm. Charge density plots revealed a charge transfer mechanism indicating the more ionic nature of the Ba–O bond compared to that of Zr–O. The surface morphology showed uniform particle dispersion with an average size of 45.31 nm. Negative phonon frequencies suggested potential structural phase transitions, and FTIR supported sample purity. Raman spectroscopy indicated second-order scattering, while XPS provided insights into surface compositions and oxidation states. UV-Vis spectroscopy showed a reduced bandgap energy of 3.08 eV, enhancing photocatalytic potential, with a degradation efficiency of 36.41% for rhodamine B under visible light. Photo-luminescence spectra displayed intense violet emission at 420.57 nm. Combining DFT simulations with extensive experimentation, this study highlights $BaZrO_3$'s tailored properties, and promising applications in photocatalysis and violet-bluish LEDs. Further research could amplify $BaZrO_3$'s capabilities.

Our study presents a novel synthesis method for $BaZrO_3$, enabling precise control over particle size and morphology while addressing scalability challenges. Using advanced techniques like UV-spectroscopy and DFT analysis, we demonstrated the ability to fine-tune the bandgap, significantly enhancing $BaZrO_3$'s potential applications in electronics and catalysis.

Author contributions

SD contributed to the conceptualization, investigation, writing original draft and data curation, VK contributed to DFT investigation and reviewing and editing, KD and CS contributed to investigation, AM contributed to synthesis, UKG and RKS contributed to XPS measurement and validation, GP contributed to methodology, supervision and reviewing, FZH contributed to the resources and validation, and NKG contributed to the supervision and reviewing of the manuscript.

Data availability

The datasets produced and/or scrutinized throughout the present study can be obtained by reaching out to the corresponding author upon a reasonable request.

Conflicts of interest

We declare that we have no competing interests.

Acknowledgements

References

1 N. Baig, I. Kammakakam, W. Falath and I. Kammakakam, *Nanomaterials: A review of synthesis methods, properties, recent progress, and challenges*, *Mater. Adv.*, Royal Society of Chemistry, 2021, vol. 2, pp. 1821–1871.

2 A. Tarafder, K. Annapurna, R. Saikia Chaliha, V. S. Tiwari, P. K. Gupta and B. Karmakar, Structure, dielectric and optical properties of Nd3+-doped LiTaO3 transparent ferroelectric glass-ceramic nanocomposites, *J. Alloys Compd.*, 2010, **489**(1), 281–288.

3 I. H. Lone, J. Aslam, N. R. E. Radwan, A. H. Bashal, A. F. A. Ajlouni and A. Akhter, *Multiferroic ABO3 Transition Metal Oxides: a Rare Interaction of Ferroelectricity and Magnetism*, *Nanoscale Res. Lett.*, Springer, New York LLC, 2019, vol. 14.

4 A. T. Mulder, N. A. Benedek, J. M. Rondinelli and C. J. Fennie, Turning ABO3 antiferroelectrics into ferroelectrics: Design rules for practical rotation-driven ferroelectricity in double perovskites and A3B2O7 Ruddlesden-popper compounds, *Adv. Funct. Mater.*, 2013, **23**(38), 4810–4820.

5 H. Labrim, Y. Selmani, S. Ziti, S. Idrissi, R. El Bouayadi, D. Zejli, *et al.*, Study of the perovskites CaZrO3-xSx (x=0, 1, 2 and 3) for photovoltaic applications, *Solid State Commun.*, 2023, **363**, 115105.

6 A. S. Patra, M. S. Chauhan, S. Keene, G. Gogoi, K. A. Reddy, S. Ardo, *et al.*, Combined Experimental and Theoretical Insights into the Synergistic Effect of Cerium Doping and Oxygen Vacancies in BaZrO 3-δ Hollow Nanospheres for Efficient Photocatalytic Hydrogen Production, *J. Phys. Chem. C*, 2019, **123**(1), 233–249.

7 Y. Parganiha, J. Kaur, V. Dubey, R. Shrivastava and S. J. Dhoble, Synthesis and luminescence study of BaZrO3:Eu3+ phosphor, *Superlattices Microstruct.*, 2015, **88**, 262–270.

8 G. Chen, F. Yu, X. Hou, J. Liu, Y. Yang, E. Wang, *et al.*, BaZrO3 refractory crucibles for vacuum induction melting of industrial Zr-based bulk metallic glass master alloys with Y addition, *J. Eur. Ceram. Soc.*, 2022, **42**(8), 3644–3651.

9 C. Kayathiri, A. R. Balu, M. Suganya, G. Vinitha, Z. Delci, S. Balamurugan, *et al.* BaZrO3 perovskite – A UV light mediated congo red dye deactivator catalyst with good optical switching and antimicrobial abilities green synthesized using Moringa oleifera leaf extract, *Mater. Sci. Eng., B*, 2022, **278**, 115636.

10 H. Niu, Y. Jing, Y. Sun, L. Guo, N. R. Aluru, W. Li, *et al.*, On the anomalous diffusion of proton in Y-doped BaZrO3 perovskite oxide, *Solid State Ionics*, 2022, **376**, 115859.

11 H. Uehara, A. Ishii, I. Oikawa and H. Takamura, Preparation and mixed proton-hole conductivity of barium zirconate doped with scandium and cobalt, *Int. J. Hydrogen Energy*, 2022, **47**(8), 5577–5584.

12 K. Zhu, N. Shi, L. Zhang, D. Huan, X. Li, X. Zhang, *et al.*, Engineering oxygen vacancy to accelerate proton conduction in Y-doped BaZrO3, *Ceram. Int.*, 2023, **49**(9), 13321–13329.

13 A. K. Arora, V. S. Jaswal, K. Singh and R. Singh, *Applications of metal/mixed metal oxides as photocatalyst: A review*, *Orient. J. Chem.*, Oriental Scientific Publishing Company, 2016, vol. 32, pp. 2035–2042.

14 H. Dai, H. Kou, H. Wang and L. Bi, Electrochemical performance of protonic ceramic fuel cells with stable BaZrO3-based electrolyte: A mini-review, *Electrochem. Commun.*, 2018, **96**, 11–15.

15 S. Akhtar, S. M. Alay-e-Abbas, J. Batool, W. Zulfiqar, A. Laref, G. Abbas, *et al.*, Investigation of structural, electronic and optical properties of (V + P)-doped BaZrO3 for photocatalytic applications using density functional theory, *J. Phys. Chem. Solids*, 2020, **147**, 109662.

16 M. L. Moreira, J. Andrés, J. A. Varela and E. Longo, Synthesis of fine micro-sized BaZrO3 powders based on a decaoctahedron shape by the microwave-assisted hydrothermal method, *Cryst. Growth Des.*, 2009, **9**(2), 833–839.

17 P. Charoonsuk, R. Baitahe, W. Vittayakorn, N. Atiwongsangthong, R. Muanghua, P. Seeharaj, *et al.* Synthesis of monodispersed perovskite barium zirconate (BaZrO3) by the sonochemical method, *Ferroelectrics*, 2013, **453**(1), 54–61.

18 A. Nyabadza, É. McCarthy, M. Makhesana, S. Heidarinassab, A. Plouze and M. Vazquez, *et al.*, *A review of physical, chemical and biological synthesis methods of bimetallic nanoparticles and applications in sensing, water treatment, biomedicine, catalysis and hydrogen storage*, *Adv. Colloid Int. Sci.*, Elsevier B.V., 2023, vol. 321.

19 B. R. Cuenya, Synthesis and catalytic properties of metal nanoparticles: Size, shape, support, composition, and oxidation state effects, *Thin Solid Films*, 2010, **518**(12), 3127–3150.

20 H. M. N. Ullah, M. Rizwan, S. S. Ali, Z. Usman and C. Cao, A DFT study of optical, elastic, mechanical, and overall

water-splitting photocatalytic properties of pristine and Cd substituted BaZrO3: A lead free environment friendly material, *Mater. Sci. Eng., B*, 2022, **286**, 116041.

21 B. B. Adormaa, W. K. Darkwah and Y. Ao, *Oxygen vacancies of the TiO2 nano-based composite photocatalysts in visible light responsive photocatalysis*, *RSC Adv.*, Royal Society of Chemistry, 2018, vol. 8, pp. 33551–33563.

22 D. Glass, R. Quesada-Cabrera, S. Bardey, P. Promdet, R. Sapienza, V. Keller, *et al.*, Probing the Role of Atomic Defects in Photocatalytic Systems through Photoinduced Enhanced Raman Scattering, *ACS Energy Lett.*, 2021, **6**(12), 4273–4281.

23 K. Nakashima, I. Fujii and S. Wada, Preparation of BaZrO 3 cubes by composite-hydroxide-mediated approach at low temperature, *J. Ceram. Soc. Jpn.*, 2011, **119**, 532–534.

24 J. Thomas, P. K. Anitha, T. Thomas and N. Thomas, BaZrO3 based non enzymatic single component single step ceramic electrochemical sensor for the picomolar detection of dopamine, *Ceram. Int.*, 2022, **48**(5), 7168–7182.

25 Y. Yuan, Z. Zhao, J. Zheng, M. Yang, L. Qiu, Z. Li, *et al.*, Polymerizable complex synthesis of BaZr1-xSnxO 3 photocatalysts: Role of Sn4+ in the band structure and their photocatalytic water splitting activities, *J. Mater. Chem.*, 2010, **20**(32), 6772–6779.

26 G. Kresse and J. Furthmüller, Efficiency of ab-initio total energy calculations for metals and semiconductors using a plane-wave basis set, *Comput. Mater. Sci.*, 1996, **6**(1), 15–50.

27 J. P. Perdew, K. Burke and M. Ernzerhof, Generalized Gradient Approximation Made Simple, *Phys. Rev. Lett.*, 1996, **77**(18), 3865–3868.

28 T. Thananatthanachon, Synthesis and Characterization of a Perovskite Barium Zirconate (BaZrO3): An Experiment for an Advanced Inorganic Chemistry Laboratory, *J. Chem. Educ.*, 2016, **93**(6), 1120–1123.

29 S. Parida, S. K. Rout, L. S. Cavalcante, E. Sinha, M. S. Li, V. Subramanian, *et al.*, Structural refinement, optical and microwave dielectric properties of BaZrO3, *Ceram. Int.*, 2012, **38**(3), 2129–2138.

30 S. Dubey, K. Dubey, V. Sahu, A. Modi, G. Pagare, F. Z. Haque, *et al.*, Exploring structural, vibrational, optical and photoluminescence characteristic of tetragonal-tungsten bronze Ba4Bi2Fe2Nb8O30 compound, *J. Mater. Sci.: Mater. Electron.*, 2023, **34**(36), 2312.

31 K. Dubey, S. Dubey, A. Modi, R. K. Sharma, S. Chakravarty, C. Parvathiraja, *et al.*, Purple-blue luminescence and magnetic properties of visible-light active novel BiMn2O5 photocatalyst by ultrasonication assisted sol–gel method, *Appl. Phys. A: Mater. Sci. Process.*, 2023, **129**(10), 715.

32 S. Dubey, J. A. Abraham, K. Dubey, V. Sahu, A. Modi, G. Pagare, *et al.*, DFT study of RhTiP half Heusler semiconductor: Revealing its mechanical, optoelectronic, and thermoelectric properties, *Phys. B*, 2024, **672**, 415452.

33 Y. Parganiha, J. Kaur, V. Dubey, R. Shrivastava and S. J. Dhoble, Synthesis and luminescence study of BaZrO3:Eu3+ phosphor, *Superlattices Microstruct.*, 2015, **88**, 262–270.

34 A. K. Kunti, N. Patra, R. A. Harris, S. K. Sharma, D. Bhattacharyya, S. N. Jha, *et al.*, Local Structure and Spectroscopic Properties of Eu3+-Doped BaZrO3, *Inorg. Chem.*, 2019, **58**(5), 3073–3089.

35 A. Babu, D. Tirumalarao, S. Das, V. Dixit, S. P. Sruthy, V. Vijayan, *et al.*, Effect of pH variation on citrate nitrate sol-gels obtained from auto-combustion method: Synthesis, calculations and characterisations of extremely dense BaZrO3 ceramic, *Open Ceram.*, 2022, **12**, 100303.

36 L. A. Morales, G. Sierra-Gallego, C. A. Barrero and O. Arnache, Relative recoilless F-factors in REFeO (RE = rare-earth La, Pr, Nd and Sm) orthoferrites synthesized by self-combustion method, *Mater. Sci. Eng., B*, 2016, **211**, 94–100.

37 C. Zhu, K. Xia, G. R. Qian, C. L. Lu, W. Z. Luo, K. F. Wang, *et al.* Hydrostatic pressure induced structural instability and dielectric property of cubic BaZrO3, *J. Appl. Phys.*, 2009, **105**(4), 044110.

38 A. Perrichon, E. J. Granhed, G. Romanelli, A. Piovano, A. Lindman, P. Hyldgaard, *et al.*, Unraveling the ground-state structure of BaZrO3 by neutron scattering experiments and first-principles calculations, *Chem. Mater.*, 2020, **32**(7), 2824–2835.

39 A. Bilić and J. D. Gale, Ground state structure of BaZrO3: A comparative first-principles study, *Phys. Rev. B: Condens. Matter Mater. Phys.*, 2009, **79**(17), 174107.

40 M. A. Helal and S. Kojima, Structural instability and phase transition in BaZrO3 single crystals: Brillouin scattering and DFT study, *Mater. Sci. Eng., B*, 2021, **271**, 115314.

41 A. R. Akbarzadeh, I. Kornev, C. Malibert, L. Bellaiche and J. M. Kiat, Combined theoretical and experimental study of the low-temperature properties of BaZrO3, *Phys. Rev. B: Condens. Matter Mater. Phys.*, 2005, **72**, 205104.

42 C. Toulouse, D. Amoroso, C. Xin, P. Veber, M. C. Hatnean, G. Balakrishnan, *et al.*, Lattice dynamics and Raman spectrum of BaZrO3 single crystals, *Phys. Rev. B*, 2019, **100**, 134102.

43 J. Zheng, D. Shi, Y. Yang, C. Lin, H. Huang, R. Guo, *et al.*, Anharmonicity-induced phonon hardening and phonon transport enhancement in crystalline perovskite BaZrO3, *Phys. Rev. B*, 2022, **105**, 224303.

44 C. Ostos, L. Mestres, M. L. Martínez-Sarrión, J. E. García, A. Albareda and R. Perez, Synthesis and characterization of A-site deficient rare-earth doped BaZrxTi1-xO3 perovskite-type compounds, *Solid State Sci.*, 2009, **11**(5), 1016–1022.

45 H. P. Kumar, C. Vijayakumar, C. N. George, S. Solomon, R. Jose, J. K. Thomas, *et al.*, Characterization and sintering of BaZrO3 nanoparticles synthesized through a single-step combustion process, *J. Alloys Compd.*, 2008, **458**(1–2), 528–531.

46 P. P. Khirade, A. B. Shinde, A. Raut, S. D. Birajdar and K. M. Jadhav, Investigations on the synthesis, structural

and microstructural characterizations of Ba1-xSrxZrO3 nanoceramics, *Ferroelectrics*, 2016, **504**(1), 216–229.

47 E. Sundharam, A. K. S. Jeevaraj and C. Chinnusamy, Effect of ultrasonication on the synthesis of barium oxide nanoparticles, *J. Bionanosci.*, 2017, **11**(4), 310–314.

48 M. A. Ansari and N. Jahan, Structural and Optical Properties of BaO Nanoparticles Synthesized by Facile Coprecipitation Method, *Mater. Highlights*, 2021, **2**(1–2), 23.

49 C. W. Kee, Assignment of O-O and Mo=O Stretching Frequencies of Molybdenum/Tungsten Complexes Revisited, *J. Chem.*, 2015, **439270**, 1–10.

50 C. C. Li, S. J. Chang, J. T. Lee and W. S. Liao, Efficient hydroxylation of BaTiO3 nanoparticles by using hydrogen peroxide, *Colloids Surf., A*, 2010, **361**(1–3), 143–149.

51 S. Parida, S. K. Rout, P. K. Barhai and J. Bera, Influence of ball milling parameters on the crystallite size of Ba(Ti 1-xZr x)O3, *Ferroelectrics*, 2012, **429**(1), 22–30.

52 M. S. Chauhan, R. Kumar, A. Umar, S. Chauhan, G. Kumar, M. Faisal, *et al.*, Utilization of ZnO nanocones for the photocatalytic degradation of acridine orange, *J. Nanosci. Nanotechnol.*, 2011, **11**(5), 4061–4066.

53 J. Oliva, E. de La Rosa, L. A. Diaz-Torres, P. Salas and C. Ángeles-Chavez, Annealing effect on the luminescence properties of BaZrO3:Yb3+ microcrystals, *J. Appl. Phys.*, 2008, **104**, 023505.

54 E. C. Aguiar, A. Z. Simões, C. A. Paskocimas, M. Cilense, E. Longo and J. A. Varela, *Photoluminescence of BaZrO3 explained by a order/disorded transformation*, *J. Mater. Sci.: Mater. Electron.*, Springer Science and Business Media, LLC, 2015, vol. 26((4)), pp. 1993–2001.

55 A. Bisen, A. Satapathy, S. Parida, E. Sinha, S. K. Rout and M. Kar, Structural, optical band gap, microwave dielectric properties and dielectric resonant antenna studies of Ba (1-x)La(2x/3)ZrO3 (0 ≤ x ≤ 0.1) ceramics, *J. Alloys Compd.*, 2014, **615**, 1006–1012.

56 P. Rosander, E. Fransson, C. Milesi-Brault, C. Toulouse, F. Bourdarot, A. Piovano, *et al.*, Anharmonicity of the anti-ferrodistortive soft mode in barium zirconate BaZrO3, *Phys. Rev. B*, 2023, **108**, 014309.

57 E. Fransson, P. Rosander, P. Erhart and G. Wahnström, Understanding Correlations in BaZrO3: Structure and Dynamics on the Nanoscale, *Chem. Mater.*, 2024, **36**, 514–523.

58 I. Charrier-Cougoulic, T. Pagnier and G. Lucazeau, Raman Spectroscopy of Perovskite-Type BaCexZr1−xO3(0≤x≤1), *J. Solid State Chem.*, 1999, **142**(1), 220–227.

59 C. Xin, P. Veber, M. Guennou, C. Toulouse, N. Valle, M. Ciomaga Hatnean, *et al.*, Single crystal growth of BaZrO3 from the melt at 2700 °C using optical floating zone technique and growth prospects from BaB2O4 flux at 1350 °C, *CrystEngComm*, 2019, **21**(3), 502–512.

60 S. Agrawal, Effect of rare earth doping on optical and spectroscopic characteristics of BaZrO3:Eu3+,Tb3+ perovskites, *Methods Appl. Fluoresc.*, 2018, **6**(3), 035002.

61 T. L. Sun and X. M. Chen, Raman spectra analysis for Ba[[Mg1- xNix)1/3Nb2/3]O3 microwave dielectric ceramics, *AIP Adv.*, 2015, **5**, 017106.

62 C. Toulouse, D. Amoroso, R. Oliva, C. Xin, P. Bouvier, P. Fertey, *et al.*, Stability of the tetragonal phase of BaZrO3 under high pressure, *Phys. Rev. B*, 2022, **106**, 134102.

63 L. R. MacArio, M. L. Moreira, J. Andrés and E. Longo, An efficient microwave-assisted hydrothermal synthesis of BaZrO3 microcrystals: Growth mechanism and photoluminescence emissions, *CrystEngComm*, 2010, **12**(11), 3612–3619.

64 B. Gulen, P. Demircivi and E. B. Simsek, UV-A light irradiated photocatalytic performance of hydrothermally obtained W doped BaZrO3 catalyst against the degradation of levofloxacin and tetracycline antibiotic, *J. Photochem. Photobiol., A*, 2021, **404**, 112869.

65 D. Briggs, *Handbook of X-ray Photoelectron Spectroscopy*, ed. C. D. Wanger, W. M. Riggs, L. E. Davis, J. F. Moulder and G. E. Muilenberg, Perkin-Elmer Corp., Physical Electronics Division, Eden Prairie, Minnesota, USA, 1979, pp. 190–195, *Surf. Interf. Anal.*, 1981, 3(4), v–v.

66 R. Chatterjee, S. Saha, D. Sen, K. Panigrahi, U. K. Ghorai, G. C. Das, *et al.*, Neutralizing the charge imbalance problem in Eu3+-Activated BaAl2O4Nanophosphors: Theoretical insights and experimental validation considering K+ Codoping, *ACS Omega*, 2018, **3**(1), 788–800.

67 M. Miodyńska, B. Bajorowicz, P. Mazierski, W. Lisowski, T. Klimczuk, M. J. Winiarski, *et al.*, Preparation and photocatalytic properties of BaZrO3 and SrZrO3 modified with Cu2O/Bi2O3 quantum dots, *Solid State Sci.*, 2017, **74**, 13–23.

68 P. J. Schmitz, Characterization of the Surface of BaCO3 Powder by XPS, *Surf. Sci. Spectra*, 2001, **8**(3), 190–194.

69 H. Zhang, J. Qiao, G. Li, S. Li, G. Wang, J. Wang, *et al.*, Preparation of Ce4+-doped BaZrO3 by hydrothermal method and application in dual-frequent sonocatalytic degradation of norfloxacin in aqueous solution, *Ultrason. Sonochem.*, 2018, **42**, 356–367.

70 J. Meng, X. Fu, K. Du, X. Chen, Q. Lin, X. Wei, *et al.*, BaZrO3 hollow nanostructure with Fe(III) doping for photocatalytic hydrogen evolution under visible light, *Int. J. Hydrogen Energy*, 2018, **43**(19), 9224–9232.

71 H. Zhou, Y. Mao and S. S. Wong, Shape control and spectroscopy of crystalline BaZrO3 perovskite particles, *J. Mater. Chem.*, 2007, **17**(17), 1707–1713.

72 J. Meng, Z. Lan, Q. Lin, T. Chen, X. Chen, X. Wei, *et al.*, Cubic-like BaZrO3 nanocrystals with exposed {001}/{011} facets and tuned electronic band structure for enhanced photocatalytic hydrogen production, *J. Mater. Sci.*, 2019, **54**(3), 1967–1976.

73 H. Tan, Z. Zhao, W. b. Zhu, E. N. Coker, B. Li, M. Zheng, *et al.*, Oxygen vacancy enhanced photocatalytic activity of pervoskite SrTiO3, *ACS Appl. Mater. Interfaces*, 2014, **6**(21), 19184–19190.

74 Y. Yuan, Z. Zhao, J. Zheng, M. Yang, L. Qiu, Z. Li, *et al.*, Polymerizable complex synthesis of BaZr1-xSnxO 3 photocatalysts: Role of Sn4+ in the band structure and their photocatalytic water splitting activities, *J. Mater. Chem.*, 2010, **20**(32), 6772–6779.

75 I. Zeba, R. Jabeen, R. Ahmad, M. Shakil, M. Rafique, M. Rizwan, *et al.*, Effect of anomalous behavior of Be-doping on structural stability, bandgap and optical properties in comparison with Mg-doped BaZrO3 perovskite: insights from DFT calculations, *Opt. Quantum Electron.*, 2020, **52**, 234.

76 A. S. Patra, G. Gogoi and M. Qureshi, Ordered-Disordered BaZrO3-δ Hollow Nanosphere/Carbon Dot Hybrid Nanocomposite: A New Visible-Light-Driven Efficient Composite Photocatalyst for Hydrogen Production and Dye Degradation, *ACS Omega*, 2018, **3**(9), 10980–10991.

77 D. Kong, Y. Zheng, M. Kobielusz, Y. Wang, Z. Bai, W. Macyk, *et al.*, Recent advances in visible light-driven water oxidation and reduction in suspension systems, *Mater. Today*, 2018, **21**(8), 97–924.

78 K. Dubey, S. Dubey, V. Sahu, A. Modi, J. Bamne, F. Z. Haque and N. K. Gaur, Defects and oxygen vacancies modified properties of transition metal doped $Ce_{0.95}X_{0.05}O_2$ (X = Fe, Co, Ni) nanoparticles, *Mater. Sci. Eng., B*, 2023, **288**, 116154.

79 M. B. Sahana, C. Sudakar, A. Dixit, J. S. Thakur, R. Naik and V. M. Naik, Quantum confinement effects and band gap engineering of SnO2 nanocrystals in a MgO matrix, *Acta Mater.*, 2012, **60**(3), 1072–1078.

80 S. K. Paswan, S. Kumari, M. Kar, A. Singh, H. Pathak, J. P. Borah, *et al.*, Optimization of structure-property relationships in nickel ferrite nanoparticles annealed at different temperature, *J. Phys. Chem. Solids*, 2021, **151**, 109928.

81 K. Telmani, H. Lahmar, M. Benamira, L. Messaadia and M. Trari, Synthesis, optical and photo-electrochemical properties of NiBi2O4 and its photocatalytic activity under solar light irradiation, *Optik*, 2020, **207**, 163762.

82 L. L. Chen, B. G. Zhai and Y. M. Huang, Rendering visible-light photocatalytic activity to undoped ZnO via intrinsic defects engineering, *Catalysts*, 2020, **10**(10), 1–16.

83 A. V. Mohod, M. Momotko, N. S. Shah, M. Marchel, M. Imran, L. Kong and G. Boczkaj, Degradation of Rhodamine dyes by Advanced Oxidation Processes (AOPs) - Focus on cavitation and photocatalysis - A critical review, *Water Resources and Industry*, 2023, **30**, 100220.

84 D. P. Aarti, R. B. Basavaraj, M. B. Madhusudana Reddy, S. S. Majani, G. R. Navyashree, T. Chandrasekhar, *et al.*, Enhanced photocatalytic, photoluminescence and fingerprint properties of Dy3+ ions doped BaZrO3 nanopowders for multifunctional applications, *Inorg. Chem. Commun.*, 2024, **162**, 112255.

85 R. Jana, P. M. Rajaitha, S. Hajra and H. J. Kim, Advancements in visible-light-driven double perovskite nanoparticles for photodegradation, Micro and Nano Systems Letters, *Soc. Micro Nano Syst.*, 2023, **11**(1), 1–8.

86 R. Terki, H. Feraoun, G. Bertrand and H. Aourag, Full potential calculation of structural, elastic and electronic properties of BaZrO3 and SrZrO3, *Phys. Status Solidi B*, 2005, **242**(5), 1054–1062.

87 R. Khenata, M. Sahnoun, H. Baltache, M. Rérat, A. H. Rashek, N. Illes and B. Bouhafs, First-principle cal-culations of structural, electronic and optical properties of BaTiO3 and BaZrO3 under hydrostatic pressure, *Solid State Commun.*, 2005, **136**(2), 120–125, DOI: **10.1016/j.ssc.2005.04.004**.

88 R. Khenata, M. Sahnoun, H. Baltache, M. Rérat, A. H. Rashek, N. Illes, *et al.*, First-principle calculations of structural, electronic and optical properties of BaTiO3 and BaZrO3 under hydrostatic pressure, *Solid State Commun.*, 2005, **136**(2), 120–125.

89 S. M. Alay-E-Abbas, F. Javed, G. Abbas, N. Amin and A. Laref, Density Functional Theory Evaluation of Ceramics Suitable for Hybrid Advanced Oxidation Processes: A Case Study for Ce4+-Doped BaZrO3, *J. Phys. Chem. C*, 2019, **123**(10), 6044–6053.

90 S. Muhammad Alay-E-Abbas, S. Nazir and A. Shaukat, Formation energies and electronic structure of intrinsic vacancy defects and oxygen vacancy clustering in BaZrO3, *Phys. Chem. Chem. Phys.*, 2016, **18**(34), 23737–23745.

91 V. Mishra, A. Sagdeo, V. Kumar, M. K. Warshi, H. M. Rai, S. K. Saxena, *et al.*, Electronic and optical properties of BaTiO3 across tetragonal to cubic phase transition: An experimental and theoretical investigation, *J. Appl. Phys.*, 2017, **122**, 065105.

92 N. Kitamura, J. Akola, S. Kohara, K. Fujimoto and Y. Idemoto, Proton distribution and dynamics in Y- and Zn-doped BaZrO3, *J. Phys. Chem. C*, 2014, **118**(33), 18846–18852.

93 V. Kumar and J. Jung, Enhancement of gas sensing by doping of transition metal in two-dimensional As2C3 nanosheet: A density functional theory investigation, *Appl. Surf. Sci.*, 2022, **599**, 153941.

94 M. Rizwan, S. Aleena, M. Shakil, T. Mahmood, A. A. Zafar, T. Hussain, *et al.*, A computational insight of electronic and optical properties of Cd-doped BaZrO3, *Chin. J. Phys.*, 2020, **66**, 318–326.

95 N. Erum, M. A. Iqbal and I. Bashir, A DFT study of structural, electronic and optical properties of pristine and intrinsic vacancy defects containing barium zarconate (BaZrO3) using mBJ potential, *Phys. Scr.*, 2020, **96**, 025807.

96 G. Lopez-Candales, Z. Tang, G. J. Cruz, W. Xia, F. Jia and P. Zhang, Quasiparticle band structures of the 4d perovskite oxides SrZr O3 and BaZr O3, *Phys. Rev. B*, 2021, **104**, 195129.

97 W. Zulfiqar, S. M. Alay-E-Abbas, G. Abbas, A. Laref, J. A. Larsson and A. Shaukat, Revisiting the structural, electronic and photocatalytic properties of Ti and Zr based perovskites with meta-GGA functionals of DFT, *J. Mater. Chem. C*, 2021, **9**(14), 4862–4876.

98 B. Favelukis, S. Chakrabartty, V. Kumar, S. H. Kim, A. El-Zoka, M. Krämer, *et al.*, Improved Durability of Ti3C2Tz at Potentials above the Reversible Hydrogen Electrode by Tantalum Substitution, *Adv. Funct. Mater.*, 2023, **34**, 2309749.

99 N. Raja, D. Murali, S. V. M. Satyanarayana and M. Posselt, Y doping of BaZrO3 may lead to optimum conditions for proton conduction at operating temperature of solid oxide

fuel cells: a first principles study, *Mater. Res. Express*, 2023, **10**, 065504.

100 Y. Parganiha, J. Kaur, V. Dubey, R. Shrivastava and S. J. Dhoble, Synthesis and luminescence study of BaZrO3: Eu3+ phosphor, *Superlattices Microstruct.*, 2015, **88**, 262–270.

101 P. P. Khirade, S. D. Birajdar, A. B. Shinde and K. M. Jadhav, Room temperature ferromagnetism and photoluminescence of multifunctional Fe doped BaZrO3nanoceramics, *J. Alloys Compd.*, 2017, **691**, 287–298.

102 C. Yi, Q. Lu, Y. Wang, Y. Wang and B. Yang, Degradation of organic wastewater by hydrodynamic cavitation combined with acoustic cavitation, *Ultrason. Sonochem.*, 2018, **43**, 156–165.